Journal of Iberian Geology (2022) 48:1–28
https://doi.org/10.1007/s41513-021-00179-8

RESEARCH PAPER

Permo-Carboniferous hypabyssal magmatism in northern Portugal: the case of the Lamas de Olo microgranite and lamprophyre dykes

António João Teixeira Oliveira[1,2] · **Helena Cristina Brites Martins**[1,2] · **Helena Maria Sant'Ovaia Mendes da Silva**[1,2]

Received: 1 April 2021 / Accepted: 29 October 2021 / Published online: 19 November 2021

Abstract

During the final stages of the Variscan orogeny, several subvolcanic dykes intruded throughout NW and SW Europe. In northern Portugal, the microgranite and lamprophyre of the Lamas de Olo region constitute a local manifestation of this magmatic event. To understand their petrogenesis, field, petrographic, and bulk-rock geochemical studies were undertaken. The lamprophyre was also analyzed for the Rb–Sr, Sm–Nd, and zircon U–Pb systematics. Mineralogically, the microgranite resembles alkali-feldspar granites, while the lamprophyre is a minette. Geochemically, the felsic dyke was probably derived from an evolved crustal source, possibly uncontaminated by mantellic or young crustal influences. The results suggest that the source is similar to that of the most evolved facies of the Lamas de Olo pluton. Structurally, the emplacement of the microgranite was presumably controlled by the regional WSW–ENE fracture system. On the other hand, lamprophyre emplacement is related to the regional NNE–SSW system. Fractional crystallization is likely to have conditioned the petrogenesis of the mafic dyke while crustal contamination probably played only a minor role. Several trace element ratios suggest that the lamprophyre resulted from low-degree melting of an enriched mantle source located in the lithospheric mantle. Source enrichment was presumably caused by subduction-related materials and metasomatism triggered by carbonate-rich fluids. When compared to other late-Variscan lamprophyres, the Lamas de Olo mafic dyke shares more similarities with the calc-alkaline specimens of Western Europe. The present work corroborates previous studies concerning the hypothesis that late to post-Variscan lamprophyres may constitute a geodynamic pointer for a change in the tectonic regime.

Keywords Microgranite · Lamprophyre · Lamas de Olo · Permo-Carboniferous magmatism · Variscan Orogeny · Petrogenesis

Resumen

Durante las etapas finales de la orogenia Varisca, varios diques subvolcánicos intruyeron en amplios sectores del NW y SW de Europa. En el norte de Portugal, el microgranito y el lamprófido de la región de Lamas de Olo constituyen una manifestación local de este evento magmático. Para entender su petrogénesis, se realizaron estudios de campo, petrográficos y geoquímicos de estas rocas. También se analizó el lamprófido en cuanto a la sistemática Rb-Sr, Sm-Nd y U-Pb del circón. Mineralógicamente, el microgranito se asemeja a los granitos de feldespato alcalino, mientras que el lamprófido es una minetta. Desde el punto de vista geoquímico, el dique félsico procede probablemente de una fuente de corteza evolucionada, posiblemente no contaminada por influencias mantélicas o de corteza joven. Los resultados sugieren que la fuente es similar a la de las facies más evolucionadas del plutón de Lamas de Olo. Estructuralmente, el emplazamiento del microgranito fue presumiblemente controlado por el sistema de fracturas regional WSW-ENE. Por otro lado, el emplazamiento del lamprófido está relacionado con el sistema regional NNE-SSW. Es probable que la cristalización fraccionada haya condicionado la petrogénesis del dique máfico, mientras que la contaminación con materiales de la corteza terrestre probablemente sólo desempeñó un papel menor.

✉ António João Teixeira Oliveira
up201107754@edu.fc.up.pt

Helena Cristina Brites Martins
hbrites@fc.up.pt

Helena Maria Sant'Ovaia Mendes da Silva
hsantov@fc.up.pt

[1] Departamento de Geociências, Ambiente e Ordenamento do Território, Faculdade de Ciências, Universidade do Porto, Rua do Campo Alegre, s/n, 4169-007 Porto, Portugal

[2] Instituto de Ciências da Terra, Polo do Porto, Rua do Campo Alegre, s/n, 4169-007 Porto, Portugal

Varias relaciones de elementos traza sugieren que el lamprófido fue el resultado de la fusión a bajo grado de una fuente de manto litosférico enriquecida. El enriquecimiento de la fuente fue presumiblemente causado por materiales relacionados con la subducción y el subsecuente metasomatismo desencadenado por fluidos ricos en carbonatos. En comparación con otros lamprófidos tardovariscos, el dique máfico de Lamas de Olo comparte más similitudes con los ejemplares calcoalcalinos de Europa occidental. El presente trabajo corrobora los estudios anteriores relativos a la hipótesis de que los lamprófidos tardi-post-variscos pueden constituir un indicador geodinámico de un cambio de régimen tectónico.

Palabras clave Microgranito · Lamprófido · Lamas de Olo · Magmatismo Permo-Carbonífero · Orogenia Varisca · Petrogénesis

1 Introduction

Post-collisional settings are often accompanied by large volumes of bimodal magmatism due to the tectonic transition between compressive and extensive regimes. In Europe, the calc-alkaline to alkaline Permo-Carboniferous magmatism, which has been the target of extensive studies since it was first recognized during the late 1970s (Lorenz & Nicholls, 1976), is probably one of the best examples of post-orogenic magmatic suites. The bimodal character of this magmatic event is evidenced by the presence of contemporaneous felsic and mafic melts, the latter being usually more common (Perini et al., 2004; Orejana et al., 2008). To the north, post-orogenic igneous rocks of Late Carboniferous to Permian age can be found (i) throughout Scotland and northern England (e.g. Timmerman, 2004), (ii) along the Norwegian coast from Magerøy to Kristiansand (e.g. Kirstein et al., 2006), and (iii) in southern Sweden, on the eastern border of the Oslo Graben (e.g. Kirstein et al., 2006). To the south, in the Iberian Massif, several dykes of subvolcanic lithologies intrude into Variscan granites and older metasediments of the Central Iberian Zone (CIZ). Even though these dykes are fairly common in both Portugal and Spain, most published studies have mainly focused on the Spanish specimens (e.g. Bea et al., 1999; Lago et al., 2004; Perini et al., 2004; Scarrow et al., 2006; Orejana et al., 2008; Ubide et al., 2010; Errandonea-Martin et al., 2018; Orejana et al., 2020). Moreover, in Western Europe, the Permo-Carboniferous magmatism is widespread throughout the French Massif Central (Perini et al., 2004) and Bohemian Massif (Štemprok et al., 2014; Soder & Romer, 2018).

The felsic component of the bimodal magmatism is mainly represented by granite porphyries, microgranites, and microsyenites, which appear to have been mainly derived by crustal melting (Bonin, 1990; Sylvester, 1998). Often, these acid lithotypes constitute the final expressions of the preceding orogenic granite magmatism. Even though the felsic and mafic melts are mostly coetaneous, occasionally the former are slightly older than the latter (Villaseca et al., 2004; Orejana et al., 2008). However, the opposite has also been verified (e.g. Fernández-Suárez et al., 2006). Compositionally, the mafic portion of the Permo-Carboniferous magmatism is more diverse. Microdiorites, microgabbros, dolerites, calc-alkaline and alkaline lamprophyres are the most common elements (Orejana et al., 2008; Soder & Romer, 2018). Among these lithologies, the petrogenesis of the lamprophyres may be regarded as the most difficult to interpret. Both calc-alkaline specimens (minettes, vogesites, kersantites, and spessartites) and the alkaline counterparts (sannaites, camptonites, and monchiquites) result from mantle-derived melts whose chemical composition might have been influenced by assimilation and/or subduction-related materials (Rock, 1977, 1991). According to Timmerman (2004), in Northern Europe, most of the mafic materials were generated after two main magmatic pulses of approximately 5 million years each, at 340 and 295 Ma. In Western Europe, geochronological results also point to two separate periods of lamprophyric magma emplacement, the first at 335–315 Ma and the second at 315–285 Ma (Seifert, 2008; Štemprok et al., 2014; Soder & Romer, 2018). On the other hand, the lamprophyre dykes of the Spanish Central System (SCS) are younger, with crystallization ages ranging from 271 to 264 Ma (Scarrow et al., 2006; Orejana et al., 2020). Several theories have been proposed to explain the generation and compositional variability of these lamprophyres such as: (i) enrichment of mantle sources by the introduction of continental materials or subduction-related components (Kirstein et al., 2006; Orejana et al., 2008; Soder & Romer, 2018); (ii) decompressional melting of a metasome layer in the lithospheric mantle (Bea et al., 1999); (iii) mantle metasomatism before the emplacement of Variscan granites (Štemprok et al., 2014); and (iv) development of a mantle plume before the opening of the Atlantic Ocean (Doblas et al., 1998). Most studies suggest that heterogeneities regarding the source regions, partial melting conditions, and type of residual phases are responsible for the distinct geochemical signatures. Orejana et al. (2008) noted that the Lower Permian mafic melts of Northwestern and Southwestern Europe present clear geochemical differences and suggested that these could be explained assuming a significant separation between the two regions at that time, until later when they were assembled during the Mid Permian (following the model of Muttoni et al., 2003).

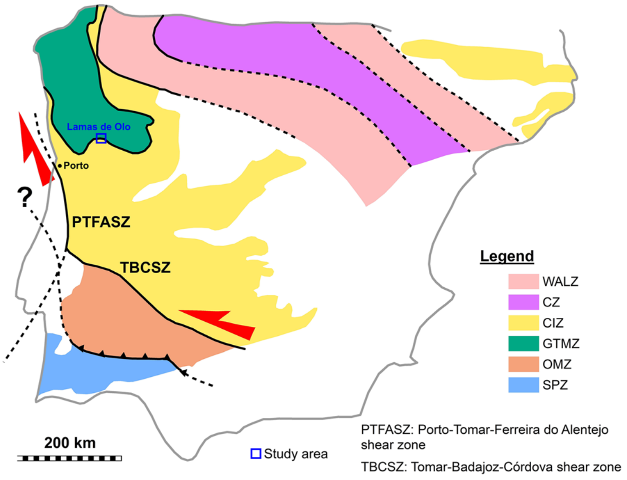

Fig. 1 Location of Lamas de Olo in the Iberian Massif setting (adapted from Dias et al., 2016). Geotectonic zones: *WALZ* - West Asturian-Leonese Zone; *CZ* - Cantabrian Zone; *CIZ* - Central Iberian Zone; *GTMZ* - Galicia-Trás-os-Montes Zone; *OMZ* - Ossa-Morena Zone; *SPZ* South Portuguese Zone

Several late to post-tectonic granite magmas were emplaced in the CIZ during the final stages of the Variscan orogeny. Afterward, when the tectonic setting shifted into an extensional regime, a subvolcanic magmatic event occurred. In the Iberian Massif, this hypabyssal event is materialized in dykes and masses of rhyolitic porphyries, dolerites, and lamprophyres. The present study focuses on the microgranite and lamprophyre dykes of the Lamas de Olo region, in northern Portugal. We present field results, petrographic description, and bulk-rock geochemical data of both lithologies, as well as isotope analyses and age constraints about the mafic dyke. The results were also compared to the published data concerning the Lamas de Olo pluton because some kind of relationship between the pluton, microgranite, and lamprophyre had been previously proposed but never fully analyzed (Pereira, 1989). Based on all information and research, we provide several petrogenetic interpretations, mainly referring to the lamprophyre. Furthermore, we discuss the main differences between the Lamas de Olo lamprophyre and similar rocks of the Variscan belt.

2 Geological Setting

The geochemistry and geochronology of several mafic, plutonic and subvolcanic rocks in the Spanish Central System (which is part of the Central Iberian Zone) were studied by Orejana et al. (2020). In their work, the generation of these lithologies is attributed to four main magmatic episodes: (i) the Ordovician rifting that led to the Rheic Ocean opening; (ii) the collisional event associated with the Variscan orogeny; (iii) the post-collisional Permian extension; and (iv) the Triassic–Jurassic rifting preceding the Atlantic Ocean opening. In the context of the present paper, only the second and third episodes are relevant. The former is represented by gabbros, diorites, and microdioritic (as well as monzonitic) dykes which were presumably derived from a lithospheric mantle reservoir, variably enriched by subduction-related fluids or melts during the Cadomian cycle. On the other hand, the third episode is associated with alkaline dykes (dolerites and lamprophyres to monzosyenitic porphyries) whose petrogenesis has been related to the melting of asthenospheric sources that were metasomatized by volatile-alkali-rich melts derived from subducted oceanic components (Orejana et al., 2020 and references therein).

The Lamas de Olo region is located in northern Portugal, about 100 km to the ENE of Porto (Fig. 1). Geotectonically, Lamas de Olo is situated near the limit between the autochthonous terrains of the Central Iberian Zone and the allochthonous and parautochthonous units of the Galicia and Trás-os-Montes Zone (Pereira, 1989). In this region, the most remarkable aspect of the local geology is the Lamas de Olo pluton (also known as LOP) which has been the subject of numerous studies (*e.g.* Pereira, 1989; Helal, 1992; Fernandes et al., 2013; Cruz et al., 2020; Cruz, 2020). The pluton is *ca*. 138 km^2, post-tectonic, and presents a rhombus-like shape, as well as three distinct composing facies. The granitic facies are known as the Lamas de Olo (LO), Barragem (BA), and Alto dos Cabeços (AC) granites. All facies are porphyritic, LO is medium to coarse-grained and biotite-rich, AC is medium to fine-grained and biotite-rich, and BA is fine to medium-grained, biotite and muscovite-rich, and only slightly porphyritic. According to Cruz et al. (2020) and Cruz (2020), the shape of the pluton was controlled by several fracture systems whose average trends are NNW–SSE (*ca*. 150° E), NNE–SSW (*ca*. N10 to 25° E), and WSW–ENE (*ca*. N80° E). Cruz (2020) demonstrated that the intersection of the WSW–ENE fault system with the NNW–SSE and NNE–SSW structures is most likely to be responsible for the emplacement of the Lamas de Olo pluton. Cruz (2020) also concluded that while the magmas that generated the Lamas de Olo and Alto dos Cabeços facies ascended along WSW–ENE fractures, the emplacement of the Barragem granite is related to the NNE–SSW fault system. The BA facies is presumably the youngest granite, as inferred from field studies (the contacts between LO and AC are mainly diffuse, but those between BA and the other granites are sharp; Cruz et al., 2020; Cruz, 2020). Geochemical data suggest that the three composing facies did not derive from the same source. While the LO and AC granites are chemically identical and presumably resulted from the same magma, the BA facies is more evolved and was generated from a different source (Cruz, 2020). Among the three facies, only Lamas de Olo has been dated: monazite analyses yield a weighted average $^{207}Pb/^{235}U$ age of 297.19 ± 0.73 Ma,

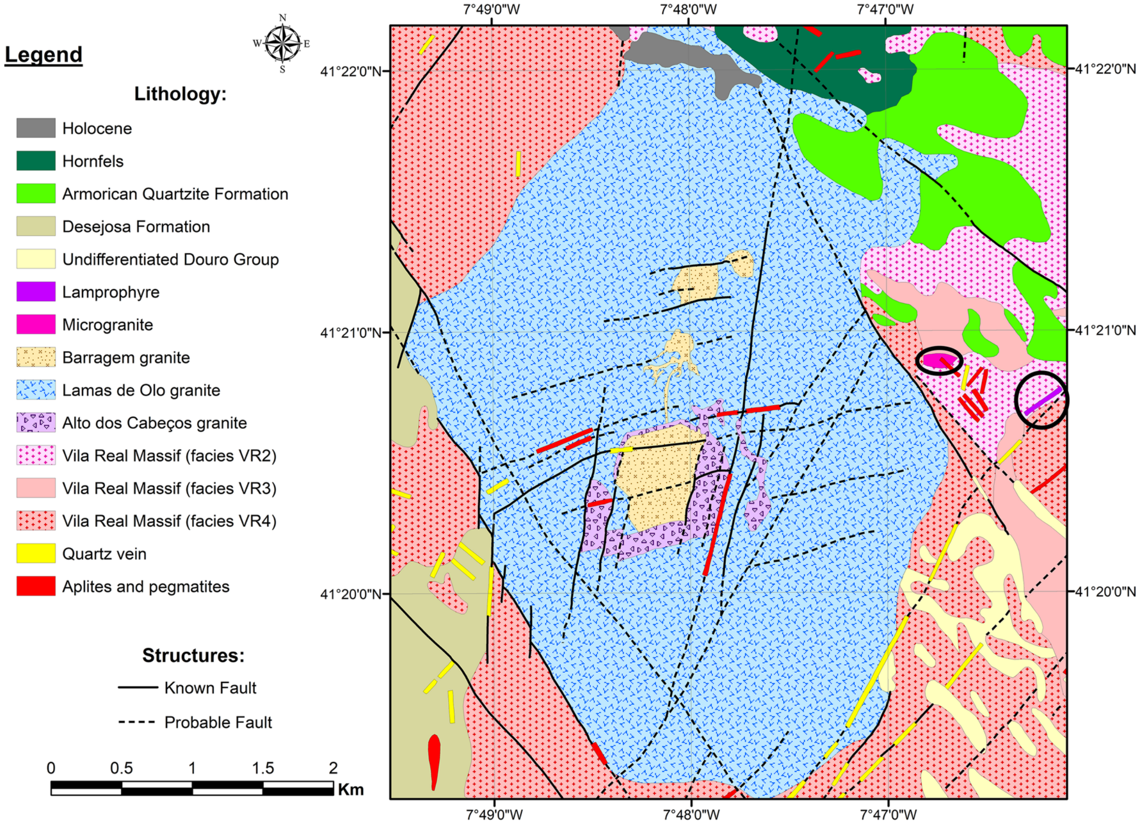

Fig. 2 Geological Map of the Lamas de Olo region (modified from Pereira et al., 1987). The Desejosa Formation and undifferentiated metasediments belonging to the Douro Group constitute different units of the Schist-Greywacke Complex. Holocene materials are composed of alluviums and sandy to loamy deposits. The black ellipses highlight the location of the studied dykes

and zircon ID-TIMS U–Pb results yield a concordia age of 296.37 ± 0.52 Ma (MSWD = 0.66) (Fernandes et al., 2013). Regarding the basement units, the pluton intrudes into several regional lithologies namely: (i) the Armorican Quartzite Formation and hornfels of Ordovician and Lower Silurian age, respectively (Pereira, 1989), to the northeast; (ii) the Desejosa Formation and other undifferentiated metasediments of the Douro Group, of Middle to Upper Cambrian age (Pereira, 1989), to the southeast, southwest, and west; and (iii) the Vila Real granitic Massif from all sides.

The microgranite and lamprophyre dykes of Lamas de Olo are located to the east of the pluton (Pereira, 1989; Oliveira et al., 2019, 2020a) (Fig. 2). The two dykes intrude into the Vila Real Massif, which is syntectonic, as well as muscovite and biotite-rich (Pereira, 1989). This Massif is composed of four distinct facies: (i) a medium to coarse-grained, porphyritic facies (hereby known as VR1); (ii) a medium to coarse-grained, slightly porphyritic facies (VR2); (iii) a fine-grained facies (VR3); and (iv) a medium to coarse-grained facies with scarce feldspar megacrysts (VR4). The two-mica granites of the Vila Real Massif yield a weighted average ^{207}Pb/^{235}U age of 311 ± 1 Ma in the Cabeceiras de Basto region (Almeida et al., 1998) and of 316 ± 7 Ma in the Carrazeda de Ansiães region (Teixeira, 2008) (both ages were determined from monazite and zircon fractions). While the microgranite is emplaced in the contact separating facies VR2 and VR3, the lamprophyre is exclusively hosted into facies VR2. The felsic dyke is E-W trending, *ca*. 230 m long, and about 1 m wide. On the other hand, the mafic lithotype is N35°E trending, *ca*. 300 m long, and 0.3 to 0.4 m wide. The contacts between the dykes and host granites are sharp.

3 Analytical Methods

Two samples of the microgranite and three samples of the lamprophyre from Lamas de Olo allowed for the study of their bulk-rock geochemistry. The geographic coordinates of the sampling sites are indicated in Table 1. Sample collection was performed with utmost care to ensure that only the freshest and least altered samples were selected for analysis. Nonetheless, the collected samples of each lithology were reasonably homogeneous.

Bulk-rock analyses were conducted at the Activation Laboratories in Ancaster (Ontario, Canada). Samples were fused

Table 1 Major, minor, and trace element contents of the Lamas de Olo microgranite and lamprophyre

Samples	MicroLO1	MicroLO2	ThetaLO1	ThetaLO2	ThetaLO3
Coordinates	41° 21′ 14.2″ N/7° 46′ 46.2″ W		41° 20′ 47.5″ N/7° 46′ 20.6″ W		
Lithology	Microgranite		Lamprophyre		
SiO_2	74.72	75.70	52.35	54.32	54.21
Al_2O_3	14.13	13.86	15.28	15.12	15.45
$Fe_2O_3^t$	0.31	0.30	7.62	6.92	7.14
MnO	0.008	0.008	0.457	0.359	0.346
MgO	0.07	0.07	5.45	5.10	5.09
CaO	0.43	0.43	3.69	3.38	2.99
Na_2O	3.24	3.25	0.60	0.45	0.36
K_2O	4.93	4.93	7.10	7.22	7.57
TiO_2	0.033	0.033	1.423	1.395	1.413
P_2O_5	0.09	0.09	1.47	1.43	1.44
LOI	1.70	1.73	4.25	3.92	4.01
Total	99.65	100.40	99.69	99.60	100.00
Sc	4	4	19	18	18
Be	5	5	18	9	9
V	< 5	< 5	142	135	140
Ba	64	64	4755	4313	4465
Sr	34	34	1235	1300	1355
Y	40	40	38	26	29
Zr	43	43	465	387	427
Cr	30	30	240	230	250
Ni	< 20	< 20	70	90	90
Zn	40	40	430	370	380
As	< 5	< 5	15	20	22
Rb	250	252	547	382	413
Nb	24	23	37	37	37
Sn	2	2	187	103	109
Cs	3.7	3.7	29.2	13.4	11.2
La	10.80	11.20	188	147	165
Ce	23.40	24.90	372	293	329
Pr	2.98	3.19	43.40	34.30	38.50
Nd	11.40	11.90	165	130	143
Sm	4.30	4.20	26.60	20.70	23.20
Eu	0.24	0.23	6.69	5.40	5.66
Gd	5.10	5.10	16.90	13.40	14.10
Tb	1.00	1.00	1.80	1.40	1.50
Dy	6.80	6.80	8.10	6.20	6.70
Ho	1.40	1.40	1.30	1.10	1.10
Er	4.00	4.20	3.50	2.70	2.80
Tm	0.63	0.67	0.46	0.37	0.38
Yb	4.20	4.50	2.80	2.30	2.40
Lu	0.64	0.70	0.38	0.36	0.34
Hf	2.5	2.4	9.9	9.7	10.1
Ta	5.2	5.3	1.7	1.7	1.7
W	2	2	50	25	21
Pb	45	48	58	128	63
Th	18.6	18.7	32.7	31.2	30.6
U	9.0	8.9	9.9	11.2	10.6
Li	NA	NA	190	140	140

Table 1 (continued)

Samples	MicroLO1	MicroLO2	ThetaLO1	ThetaLO2	ThetaLO3
Coordinates	41° 21′ 14.2″ N/7° 46′ 46.2″ W		41° 20′ 47.5″ N/7° 46′ 20.6″ W		
Lithology	Microgranite		Lamprophyre		
F	NA	NA	3500	2200	1700
ΣREE	76.89	79.99	836.93	658.23	733.68
$(La/Yb)_N$	1.73	1.68	45.27	43.09	46.35
$(La/Sm)_N$	1.58	1.68	4.45	4.47	4.47
$(Gd/Yb)_N$	0.98	0.91	4.87	4.70	4.74
$(Eu/Eu^*)_N$	0.16	0.15	0.96	0.99	0.96

Major and minor elements are expressed in weight percentage (wt%), while the trace elements are in parts per million (ppm)

in a solution of lithium metaborate and tetraborate, subsequently analyzed by ICP (Inductively Coupled Plasma) and ICP/MS (Inductively Coupled Plasma/Mass Spectrometry), diluted, and analyzed once more by a Perkin Elmer Sciex ELAN 6000, 6100, or 9000 ICP/MS equipment. For each sample, mass analysis is required as an additional quality control technique, and totals vary between 98.5% and 101%. This analytical procedure presents the following detection limits: 0.01% for major elements (Al_2O_3, CaO, Fe_2O_3, K_2O, MgO, Na_2O, P_2O_5, and SiO_2); 0.001% for minor elements (MnO and TiO_2); and 0.01–30 ppm for trace elements. Precision is 1–2% (for major and minor elements) or 20% (for trace elements) at greater than 100 times the detection limit.

Two additional methods were applied to determine lithium and fluorine contents in the lamprophyre. Lithium contents were determined using sodium peroxide fusion, while a technique based on an Ion Selective Electrode was used to know fluorine contents. The first procedure requires an initial sodium peroxide fusion, followed by acid dissolution. Next, samples were analyzed by the Perkin Elmer Sciex ELAN 6000, 6100, or 9000 ICP/MS equipment. The detection limit is 0.001%. For the second procedure, samples are fused with a mixture of lithium metaborate and lithium tetraborate in an induction furnace to release fluoride ions from the sample matrix. Afterward, the fuseate is dissolved in dilute nitric acid, the resulting solution is complexed, and finally, the ionic strength is adjusted with an ammonium citrate buffer. A fluoride ion electrode is immersed in the final solution to measure the fluoride-ion activity directly. An automated fluoride analyzer is used for the analysis. The associated detection limit is 0.01%.

The U–Pb isotope analyses for geochronological purposes were conducted in Granada, Spain, at the IBERSIMS Laboratories of the Center for Scientific Instrumentation of the University of Granada (CIC-UGR), using a multicollector Sensitive High-Resolution Ion Microprobe (SHRIMP IIe/MC). For this methodology, zircon crystals of the lamprophyre were recovered after sample crushing and sieving, density separation using a Wilfley table, and heavy liquid and magnetic separations. Hand-picking of zircon grains was done with great care to ensure the absence of fractures, inclusions, and evidence of metamictization. A fraction of 38 zircon crystals of the Lamas de Olo lamprophyre plus several standard grains were cast on an epoxymount (megamount, 3.5 cm in diameter), polished, and documented using both optical microscopy (in reflected and transmitted light) and scanning electron microscopy (based on secondary electrons and cathodoluminescence). Selected spots were rastered with a primary beam for 120 s before the analysis and then analyzed 6 scans. The primary beam, composed of single charged, double ^{16}O ions, is conventionally set to an intensity of about 5 nA, with a 120 µm Kohler aperture, which generates 17 × 20 μm^2 elliptical spots on the target. All calibration procedures were performed on the standards introduced on the same mount. The TEMORA-1 zircon (whose age is 416.8 ± 1.1 Ma; Black et al., 2003), which is used as a standard for the isotope ratios, was subsequently measured every 4 unknowns. Point-to-point errors (95% C.I.) on the TEMORA standard were ± 0.20% for $^{206}Pb/^{238}U$ and ± 0.16% for $^{207}Pb/^{206}Pb$. Data reduction and age calculations were performed using the SHRIMPTOOLS program (which is available from www.ugr.es/fbea).

The Rb–Sr and Sm–Nd isotope analyses were executed in Bilbao, Spain, at the Laboratories of General Research Service for Geochronology and Isotopic Geochemistry of the University of the Basque Country (SGIKER-UPV/EHU). The selected lamprophyre sample was analyzed by ID-MC-ICP-MS (Isotope Dilution-Multi-collector-Inductively Coupled Plasma Mass Spectrometry). About 0.050–0.200 g of the whole-rock sample was weighed and mixed with a proportional amount of an enriched ^{149}Sm-^{150}Nd tracer. The sample-tracer mixture was digested after a tri-acid attack (HF-HNO_3-$HClO_4$) following the procedures of Pin and Santos Zalduegui (1997). For strontium purification, the alkaline earth metal was isolated with a selective extraction material (Sr-resin), according to the chromatographic procedures of De Muynck et al. (2009). For samarium and neodymium purification, the chromatographic procedures of

Pin and Santos Zalduegui (1997) were followed to isolate the two LREE (light Rare Earth Elements).

For the strontium mass spectrometry, the Sr concentrate was dissolved in 2 mL of 0.32 N HNO_3 and subsequently diluted to a final concentration of approximately 200 ng Sr/g solution. The analysis of the certified reference material NBS 987 was used to verify the accuracy and reproducibility of the method. The average $^{87}Sr/^{86}Sr$ ratio of 2 determinations in this standard during the same analytical session was 0.710278, with $2\sigma = 0.000023$. For the samarium mass spectrometry, a pure Sm fraction was dissolved in 2 mL of 0.32 N HNO_3 and diluted to a final concentration of about 30 ng Sm/g solution. On the other hand, for the neodymium mass spectrometry, a pure Nd fraction was dissolved in 2 mL of 0.32 N HNO_3 and diluted to a final concentration of approximately 20 ng Nd/g solution. The certified reference material JNdi-1 was analyzed to verify the accuracy and reproducibility of the method. The average $^{143}Nd/^{144}Nd$ ratio of 2 determinations in this standard during the same analytical session was 0.512091, with $2\sigma = 0.000009$. The precision in the determination of the $^{147}Sm/^{144}Nd$ ratio by isotope dilution is typically better than 0.2%. The calculation of the $(^{87}Sr/^{86}Sr)_i$ and εNd_i parameters was based on the decay constants of Villa et al. (2015) for isotope ^{87}Rb ($\lambda = (1.397 \pm 0.003)*10^{-11}\ y^{-1}$) and of Lugmair and Marti (1978) for isotope ^{147}Sm ($\lambda = 6.54*10^{-12}\ y^{-1}$), as well as the CHUR $^{143}Nd/^{144}Nd$ and $^{147}Sm/^{144}Nd$ ratios of Jacobsen and Wasserburg (1984).

4 Results

4.1 Petrography

The petrographic study was carried out on a mesoscopic and microscopic scale. During the field sessions, the mineralogy of opaque phases was preemptively assessed through local measurements of the bulk magnetic susceptibility (K_m). A portable magnetic susceptibility meter (model Terraplus KT-10) was used for these measurements.

4.1.1 Microgranite

The Lamas de Olo microgranite is a medium to fine-grained lithology (< 0.1–0.3 cm). At hand scale, the felsic dyke is light-beige to slightly greenish. The pale coloration resulted from moderate feldspar alteration and chloritization. The texture is holocrystalline, xenomorphic to hipidiomorphic, phaneritic to microphaneritic, and heterogranular to equigranular. Quartz and potassium feldspar are the only essential minerals, while muscovite, apatite, chloritized biotite, opaque minerals, and brookite/anatase constitute accessory phases. Compositionally, this lithotype resembles alkali-feldspar granites. Occasionally, a few small granitic veinlets, 0.4–0.5 cm wide, cut through the microgranitic facies (Fig. 3a). These veinlets are slightly coarser than the microgranite (0.3–0.5 cm) and their texture is holocrystalline, phaneritic, hipidiomorphic to allotriomorphic, and equigranular or seriate. The veinlets present essential quartz, K-feldspar, and plagioclase, while muscovite, biotite, iron oxides, titanite, and garnet are accessories. The veinlet mineral paragenesis is identical to that of a syenogranite.

Potassium feldspar and quartz crystals roughly present the same size (*ca.* 100–800 μm). Their shape is mainly anhedral or anhedral to subhedral. The K-feldspar grains also have tabular habit, while the boundaries of the quartz grains are linear, curved, or wavy. The Lamas de Olo microgranite exhibits abundant intergrowths of these minerals in micrographic and granophyric textures (Fig. 3b) which are seemingly arranged in radial shapes (Fig. 3c). Kaolinization has masked most textural features of the alkali-feldspar, namely the Karlsbad twinning and venule-type perthites. On the other hand, quartz reveals incipient undulatory extinction (Fig. 3d) and rare polygranular aggregates. Considering both the alteration and textural elements, K-feldspar in the microgranite is mostly orthoclase.

Muscovite is essentially primary. The white mica grains are *ca.* 50–200 μm long and mainly present an anhedral shape and tabular or lamellar habit. Occasionally, muscovite crystals reveal weak cleavage bending (Fig. 3e). Also, rare symplectites can be seen in the boundaries with quartz grains. Apatite crystals are mostly *ca.* 50–100 μm long, prismatic, and anhedral or subhedral. The small mode of biotite in this lithology is consistent with the low bulk magnetic susceptibility values registered on the field: $K_m = 0.898–2.844$ μSI. The dark mica crystals present an elongated lamellar habit and subhedral or anhedral shape. Biotite is commonly intensely altered to both chlorite and brookite/anatase (the latter present an anhedral or euhedral shape and prismatic or elongated habit; Fig. 3f). The opaque minerals occur in grains of subhedral or anhedral shape and elongated prismatic habit. Considering the results of the magnetic susceptibility measurements, these opaque crystals are paramagnetic (and possibly composed of ilmenite). No fresh plagioclase crystals were observed in the microgranite. If plagioclase exists in this lithology, all grains are completely altered to sericite. However, in the granitic veinlets, plagioclase is a frequent accessory mineral (Fig. 3g). The iron oxides are rare secondary minerals that were also only observed in the granitic veinlets. These minerals (hematite and goethite) manifest in irregular or anhedral, orange-reddish masses. Titanite and garnet are extremely rare and their crystals are euhedral. Titanite is completely altered to leucoxene (Fig. 3h).

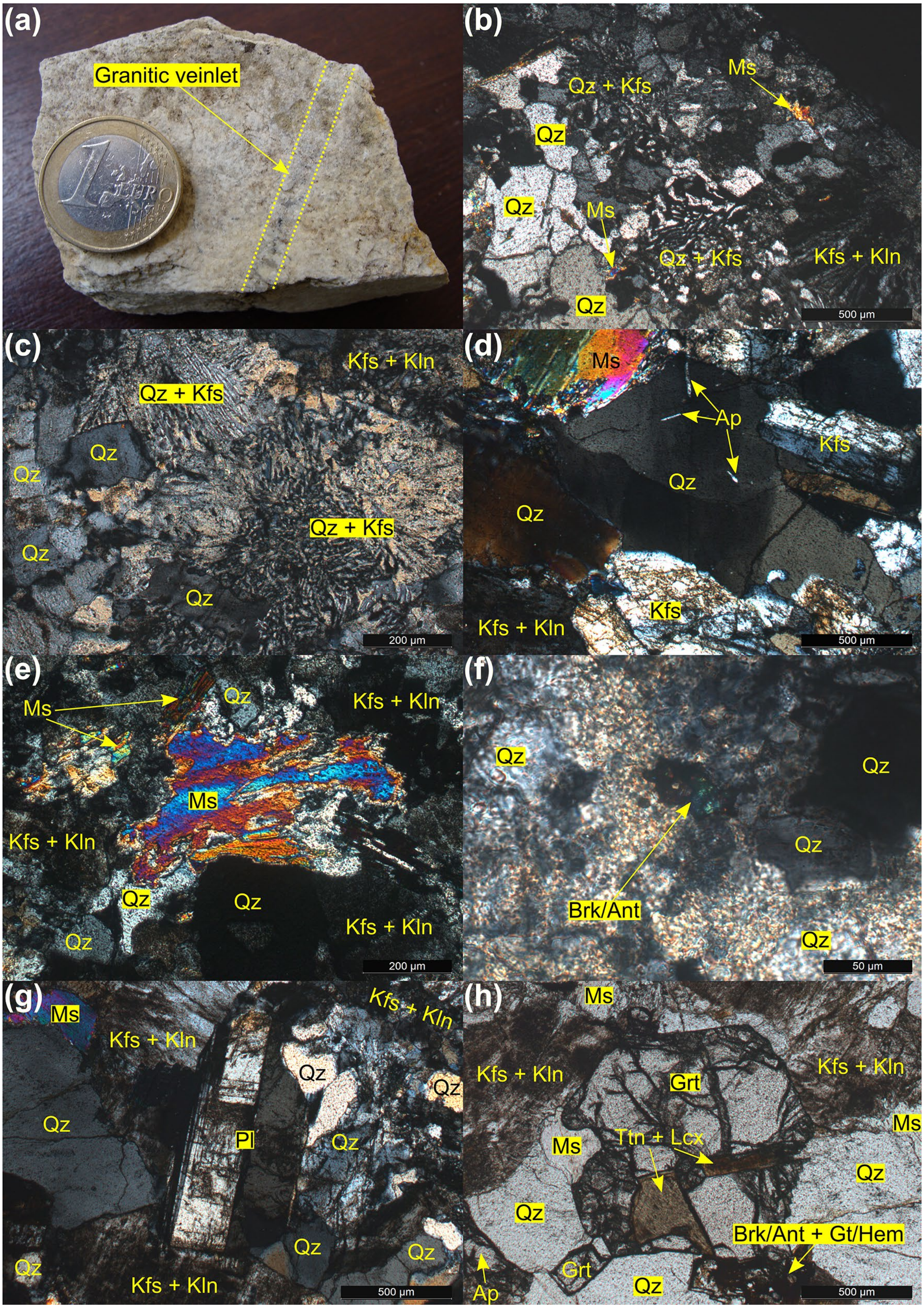
(a)
Granitic veinlet
(b)
Qz + Kfs
Ms
Qz
Qz
Ms
Qz + Kfs
Kfs + Kln
Qz
500 µm
(c)
Kfs + Kln
Qz + Kfs
Qz
Qz
Qz + Kfs
Qz
Qz
200 µm
(d)
Ms
Ap
Kfs
Qz
Qz
Kfs
Kfs + Kln
500 µm
(e)
Ms
Qz
Kfs + Kln
Ms
Kfs + Kln
Qz
Qz
Kfs + Kln
Qz
200 µm
(f)
Qz
Qz
Qz
Brk/Ant
Qz
50 µm
(g)
Ms
Kfs + Kln
Kfs + Kln
Qz
Qz
Qz
Pl
Qz
Qz
Qz
Qz
Kfs + Kln
500 µm
(h)
Ms
Kfs + Kln
Grt
Kfs + Kln
Ms
Ms
Ttn + Lcx
Qz
Qz
Brk/Ant + Gt/Hem
Ap
Grt
Qz
500 µm

◂**Fig. 3** Petrographic photographs and microphotographs of the Lamas de Olo microgranite: **a** - hand sample showcasing a small granitic veinlet; **b** - micrographic and granophyric intergrowths of quartz and potassium feldspar; **c** - intergrowth arrangement in radial shapes; **d** - undulatory extinction of veinlet quartz crystals with multiple apatite inclusions; **e** - weak cleavage bending on muscovite; **f** - highlight of a brookite/anatase crystal; **g** - undeformed plagioclase crystal of the granitic veinlets cutting through the microgranite; **h** - highlight of garnet and titanite in the granitic veinlets. Legend: *Qz* - quartz; *Kfs* - potassium feldspar; *Pl* - plagioclase; *Ms* - muscovite; *Ap* - apatite; *Kln* - kaolinite; *Brk* - brookite; *Ant* - anatase; *Grt* - garnet; *Ttn* - titanite; *Lcx* - leucoxene; *Gt* - goethite; *Hem* - hematite. Microphotographs (**b**–**g**) were taken in CPL (cross-polarized light), while microphotograph (**h**) was taken in PPL (plain-polarized light)

4.1.2 Lamprophyre

The Lamas de Olo lamprophyre is a melanocratic lithology of black to dark grey color and fine granularity. Despite all care taken during the sampling stage, this rock is highly altered, as evidenced by the presence of a greenish film. The characteristic porphyritic texture is highlighted by numerous phenocrysts that occur throughout the aphanitic groundmass (Fig. 4a). The phenocrysts are 0.1–0.7 cm long and composed of biotite and amphibole. Furthermore, the Lamas de Olo lamprophyre exhibits a few quartz veinlets (< 0.1 cm wide) as well as quartz xenocrysts (0.2–0.5 cm long). Texture in this dyke is also holocrystalline, xenomorphic in the groundmass, and hipidiomorphic regarding the general phenocryst and microphenocryst habit. The mineral assemblage is rich in biotite, pyroxene, K-feldspar, plagioclase, and amphibole, while quartz, opaque minerals (magnetite + ilmenite), apatite, zircon, monazite, and iron oxides are accessory phases. Contrary to the original proposal (Pereira, 1989) and more recent re-evaluations (Oliveira et al., 2019), in this work, the Lamas de Olo lamprophyre is classified as a minette, based on the IUGS recommendations for the classification of igneous rocks (Le Maitre et al., 2002).

Biotite and pyroxene are the most common essential minerals. Biotite occurs at the groundmass level and in phenocrysts or microphenocrysts, while pyroxene is both a groundmass mineral and microphenocryst phase. Groundmass biotite grains exhibit anhedral to subhedral shape and tabular or lamellar habit, while biotite phenocrysts and microphenocrysts mostly present subhedral shape and lamellar habit. On the other hand, all pyroxene crystals reveal an elongated prismatic or tabular habit and predominant subhedral shape. In the studied lamprophyre, both K-feldspar and plagioclase are present, but the former is more abundant. Potassium feldspar occurs at the groundmass level, in crystals of tabular habit and subhedral or anhedral shape. Groundmass plagioclase grains are rarer but present a similar habit. Feldspar microphenocrysts (plagioclase only) are very scarce, tabular, and subhedral. Amphibole occurs solely in microphenocrysts and phenocrysts, exhibiting a prismatic or hexagonal habit, and subhedral to euhedral shape. Biotite is moderately altered to chlorite, whereas pyroxene is extremely altered to amphibole (due to uralitization) or biotite. The feldspars are partially or completely altered to kaolinite or sericite, thus hindering observation of the twinnings. Primary amphibole is also frequently altered to biotite due to biotitization. Concerning textures and microstructures, cleavage bending and kinks have been occasionally detected on biotite microphenocrysts (Fig. 4b), groundmass biotite, pyroxene, and plagioclase grains are frequently organized in intergranular texture (Fig. 4c), and biotite, pyroxene, and amphibole microphenocrysts are commonly associated in glomeroporphyritic texture. A few pyroxene microphenocrysts appear to have been corroded, as well as infilled by the groundmass (Fig. 4d). Also, some potassium feldspar grains reveal an unusual deformation (Fig. 4e) and rare small corrosion gulfs were seen on amphibole microphenocrysts (Fig. 4f). Based on the petrographic observations, pyroxene crystals of the Lamas de Olo lamprophyre are presumably augite (diopsidic or Ti–rich), while amphibole is possibly green or brown hornblende.

Even though quartz mainly occurs in xenocrysts, a few groundmass grains have also been identified. Both the xenocrysts and groundmass crystals present a predominant anhedral (rounded) shape and linear, curved, or wavy boundaries. The xenocrystic nature of the larger crystals was identified from the small reaction rims in the boundaries with the groundmass (Fig. 4g) and internal corrosion gulfs generating skeletal texture. Regarding textures and microstructures, undulatory extinction is weakly developed, while fractures are common. The opaque mineral grains are mostly anhedral and dispersed throughout the groundmass. However, rare opaque microphenocrysts with euhedral shape and prismatic habit (*ca*. 300–800 μm) also exist. Considering the bulk magnetic susceptibility of the lamprophyre (K_m = 431.7–1178 μSI), most opaque crystals are ferromagnetic and probably composed of magnetite. Ilmenite is possibly present as well since some samples show K_m below 1000 μSI. A few magnetite grains are altered to hematite due to martitization (Fig. 4h). Apatite crystals present prismatic habit (either elongated, needle-like, or more rounded) and euhedral or anhedral shape. The iron oxides (mainly goethite and hematite) are rare secondary mineral phases, which resulted from the alteration of primary ferromagnesian crystals, occurring in anhedral masses of orange or reddish color. Zircon and monazite are extremely rare accessory minerals whose grains are prismatic and euhedral.

4.2 Whole-rock Geochemistry

Bulk-rock compositions of the Lamas de Olo microgranite and lamprophyre dykes are indicated in Table 1. Pereira (1989) proposed the existence of some sort of relationship

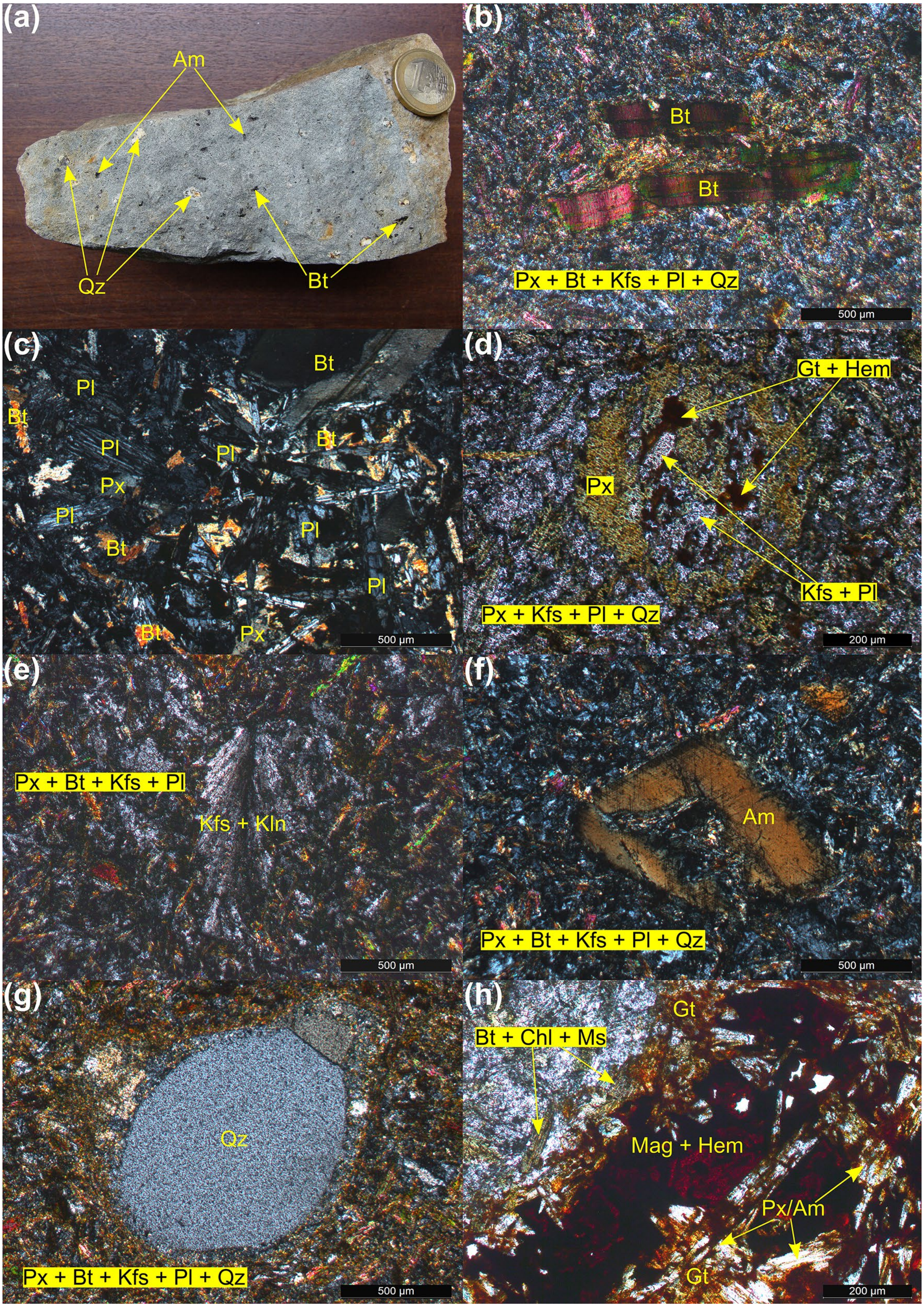

between the Lamas de Olo pluton, microgranite, and lamprophyre (as previously mentioned). For that reason, a comparative geochemical study was performed within the compass of the present article. Whole-rock geochemical data of the three facies composing the LOP were compiled from Helal (1992) and Cruz (2020).

◀**Fig. 4** Petrographic photographs and microphotographs of the Lamas de Olo lamprophyre: **a** - hand sample showcasing biotite and amphibole phenocrysts, and quartz xenocrysts; **b** - cleavage bending on biotite microphenocrysts; **c** - intergranular texture; **d** - corroded pyroxene microphenocryst infilled by the groundmass; **e** - unusual deformation of potassium feldspar grains; **f** - corrosion gulf on an amphibole microphenocryst; **g** - reaction rims around quartz xenocrysts; **h** - altered magnetite phenocrysts (martitization). Legend: *Qz* - quartz; *Kfs* - potassium feldspar; *Pl* - plagioclase; *Bt* - biotite; *Am* - amphibole; *Px* - pyroxene; *Gt* - goethite; *Hem* - hematite; *Kln* - kaolinite; *Chl* - chlorite; *Ms* - muscovite; *Mag* - magnetite. Microphotographs (**d**) and (**h**) were taken in PPL; all others were taken in CPL

4.2.1 Microgranite

On average, the Lamas de Olo microgranite dyke shows higher contents in SiO_2, K_2O, and P_2O_5, and lower contents in $Fe_2O_3^t$, Al_2O_3, MgO, CaO, TiO_2, and MnO when compared to the Lamas de Olo and Alto dos Cabeços granites. Regarding average Na_2O contents, the microgranite is slightly richer than the AC facies, but poorer when compared to the LO granite. The overall whole-rock composition of the microgranite and Barragem facies, concerning major and minor elements, are remarkably similar. Even though there are no clear evolutionary trends between the Lamas de Olo microgranite and granitic facies on Harker diagrams for Al_2O_3, K_2O, P_2O_5, MnO, and Na_2O, the contents in $Fe_2O_3^t$, MgO, CaO, and TiO_2 clearly follow a downward trend from the more primitive lithologies to the more evolved ones (Fig. 5).

The microgranite is a strongly peraluminous (ASI = 1.22–1.25) and high-K calc-alkaline rock, chemically similar to an alkali-feldspar granite (Fig. 6a and b). It is also magnesian (Fe* = 0.79–0.80), calc-alkalic to alkali-calcic (MALI = 7.74–7.75%), and highly felsic peraluminous (Figs. 6c and 7a). The geochemical results suggest that the generation of the Lamas de Olo microgranite is associated with a transitional, post-orogenic, or anorogenic tectonic setting (Figs. 6d, 7b, and c). Furthermore, the Lamas de Olo, Barragem, and Alto dos Cabeços granites are also peraluminous and high-K calc-alkaline. However, while LO and AC are only weakly to moderately peraluminous (LO: ASI = 1.05–1.14; AC: ASI = 1.08–1.31) and their chemistry is typical of orogenic and late to post-orogenic settings, BA is, like the microgranite, highly felsic peraluminous (ASI = 1.11–1.24) and mainly associated with post-orogenic and anorogenic settings.

Considering the average trace element contents, when compared to all three granites the microgranite is poorer in Ba, Zr, Be, Cs, and Hf, and richer in Y and Pb. The Lamas de Olo microgranite is also enriched in Nb and Ta in regard to the LO and AC facies, while these granites present higher Sr contents. On the other hand, the microgranite is richer in Rb and Th, as well as poorer in U, than the Lamas de Olo facies; the exact opposite is verified when the felsic dyke is compared to the Alto dos Cabeços granite. Once again, the microgranite and Barragem facies are compositionally similar. On Harker diagrams, some trace elements (namely Ba, Sr, Zr, Ta, and Pb) define apparent linear trends between the microgranite samples and pluton facies (Fig. 8). Unlike the case of the Vila Pouca de Aguiar porphyries (Oliveira et al., 2020b), the Lamas de Olo microgranite does not exhibit any specific enrichment in rare incompatible metal elements.

The Rare Earth Element (REE) contents of the Lamas de Olo microgranite are low (ΣREE = 76.89–79.99 ppm). When compared to the LO and AC granites, this lithology is clearly depleted in these elements. However, the REE contents of the BA facies are similar to those of the microgranite. The respective REE spectra are presented in Fig. 9. The microgranite profiles exhibit very weak general fractionations ($(La/Yb)_N = 1.68–1.73$), a slight LREE fractionation ($(La/Sm)_N = 1.58–1.68$), an almost flat MREE-HREE pattern ($(Gd/Yb)_N = 0.91–0.98$; MREE and HREE are the medium and heavy REE, respectively), and negative, strong Eu anomalies ($(Eu/Eu^*)_N = 0.15–0.16$). Regarding the spectra of the granitic facies, the profiles of the Lamas de Olo and Alto dos Cabeços granites are discordant when compared to the microgranite spectra, but the Barragem profiles are identical.

Multi-element spidergrams of the microgranite and granitic facies composing the Lamas de Olo pluton are illustrated in Fig. 10. The three granites and the felsic dyke exhibit identical anomalies, which are consistently more pronounced in the BA facies and microgranite profiles. The multi-element spectra of the Lamas de Olo microgranite reveal clear positive anomalies in Rb, Cs, Ta, Pb, Th, and U, weak positive anomalies in P, and evident negative anomalies in Ti, Zr, Nb, Ba, and REE. When comparing the spidergrams of the microgranite and Barragem granite, the latter reveals stronger anomalies in U and Ta.

4.2.2 Lamprophyre

The Lamas de Olo lamprophyre is a mafic lithology of intermediate to basic composition, whose magnesium and sodium contents are, respectively, low and very low. However, the contents in other major and minor elements (such as Al_2O_3, $Fe_2O_3^t$, CaO, K_2O, TiO_2, P_2O_5, and MnO) are high. Even though #Mg values are moderately significant (#Mg ≈ 0.59), they do not reflect a primitive nature for the lamprophyric magma according to the criteria of Frey et al. (1978) (*i.e.* #Mg > 0.6–0.7). The #Mg parameter was calculated using the following equation: $\#Mg = \frac{(MgO/40.305)}{(MgO/40.305)+(FeO^t/71.845)}$, where 40.305 and 71.845 are the molar masses for MgO and FeO.

The Lamas de Olo mafic dyke is metaluminous to weakly peraluminous (A/CNK = 0.99–1.09), ultrapotassic (K_2O/

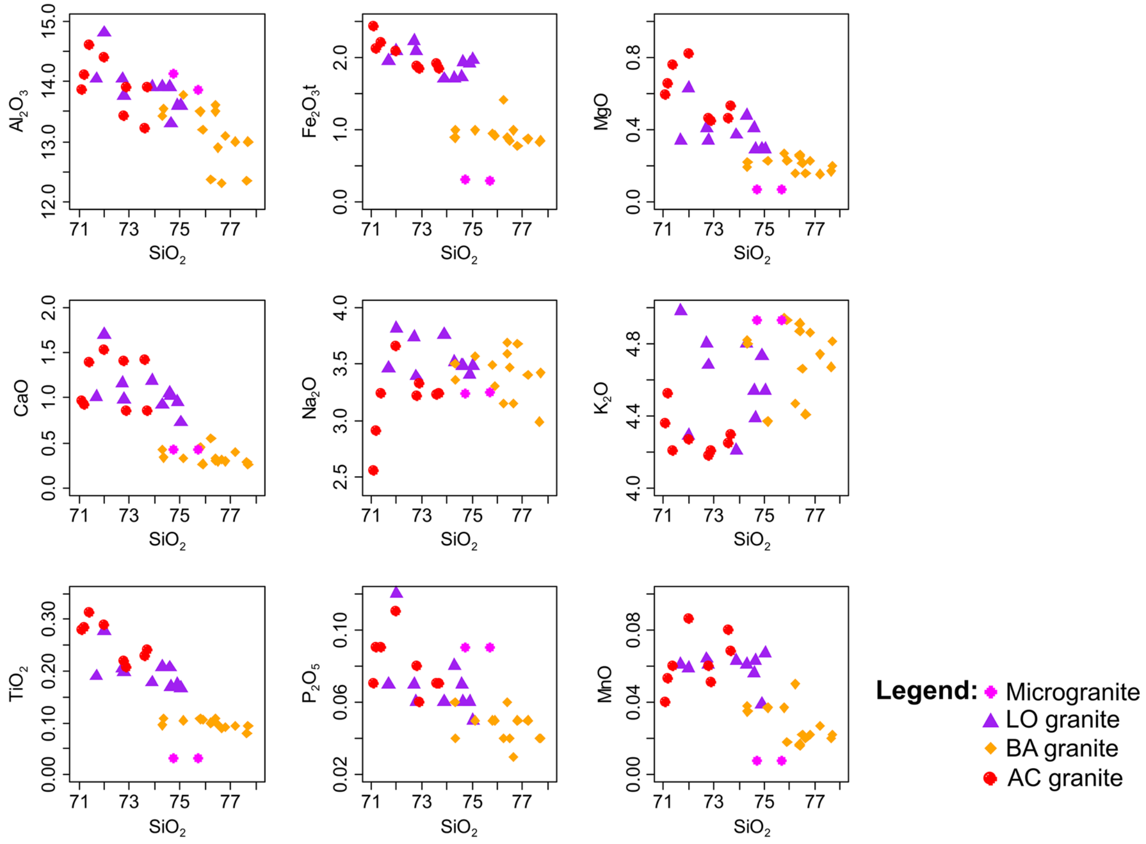

Fig. 5 Harker diagrams for major and minor elements of the microgranite and granitic facies of the Lamas de Olo pluton. LOP granite data after Helal (1992) and Cruz (2020)

Na_2O = 11.83–21.03), shoshonitic, and chemically equivalent to monzonites, monzodiorites, and/or quartzmonzonites (Fig. 6a and b). According to the classification of Foley et al. (1987), this lamprophyre is plotted within the Group III field of ultrapotassic rocks (Fig. 11a), which is exclusively associated with orogenic settings. On the other hand, on the Sm versus Ce/Yb diagram of Rock (1991), the mafic dyke is plotted on the alkaline field, next to the boundary with the lamproites field (Fig. 11b). When considering the Aluminum Saturation Index over the A/CNK ratio, the Lamas de Olo lamprophyre is also peraluminous (ASI = 1.12–1.24), which attests to the remarkable amount of apatite (Fig. 6c). The two ratios are different because the ASI also takes into account the calcium that was incorporated into apatite (Frost et al., 2001). Based on the geochemical data, the studied lamprophyre is tectonically associated with late to post-collisional settings (Figs. 6d, 11c and d).

Unlike the microgranite, the lamprophyre presents very high REE contents (ΣREE = 658.23–836.93 ppm), which is related to the remarkable amount of minerals capable of concentrating these elements (such as pyroxene, amphibole, apatite, zircon, and monazite). The lamprophyre REE spectra (Fig. 9) are highly fractionated ($(La/Yb)_N$ = 43.09–46.35) and reveal fairly similar LREE and HREE fractionations ($(La/Sm)_N$ = 4.45–4.47; $(Gd/Yb)_N$ = 4.70–4.87). However, the Eu anomalies are virtually non-existent ($(Eu/Eu^*)_N$ = 0.96–0.99).

Multi-element spidergrams of the mafic dyke are illustrated in Fig. 10. The subvolcanic rock reveals positive anomalies in Rb, Cs, Ba, LREE, Th, and U, as well as negative anomalies in Sr and most HFSE (Ti, Zr, Nb, Ta). Lead anomalies are markedly positive, while phosphorus anomalies are weakly positive.

4.3 Geochronology and Isotope Geochemistry

A fraction of 38 hand-picked zircon crystals of the Lamas de Olo lamprophyre allowed for the study and calculation of U–Pb ages. Typologically, the lamprophyre zircons are mainly prismatic (both short and long). However, many are needle-like, and some are lamellar as well. Most crystals are euhedral, and the prismatic zircons are commonly asymmetric. Overall, the prisms are more developed than the pyramids, which are not always present. The zircons

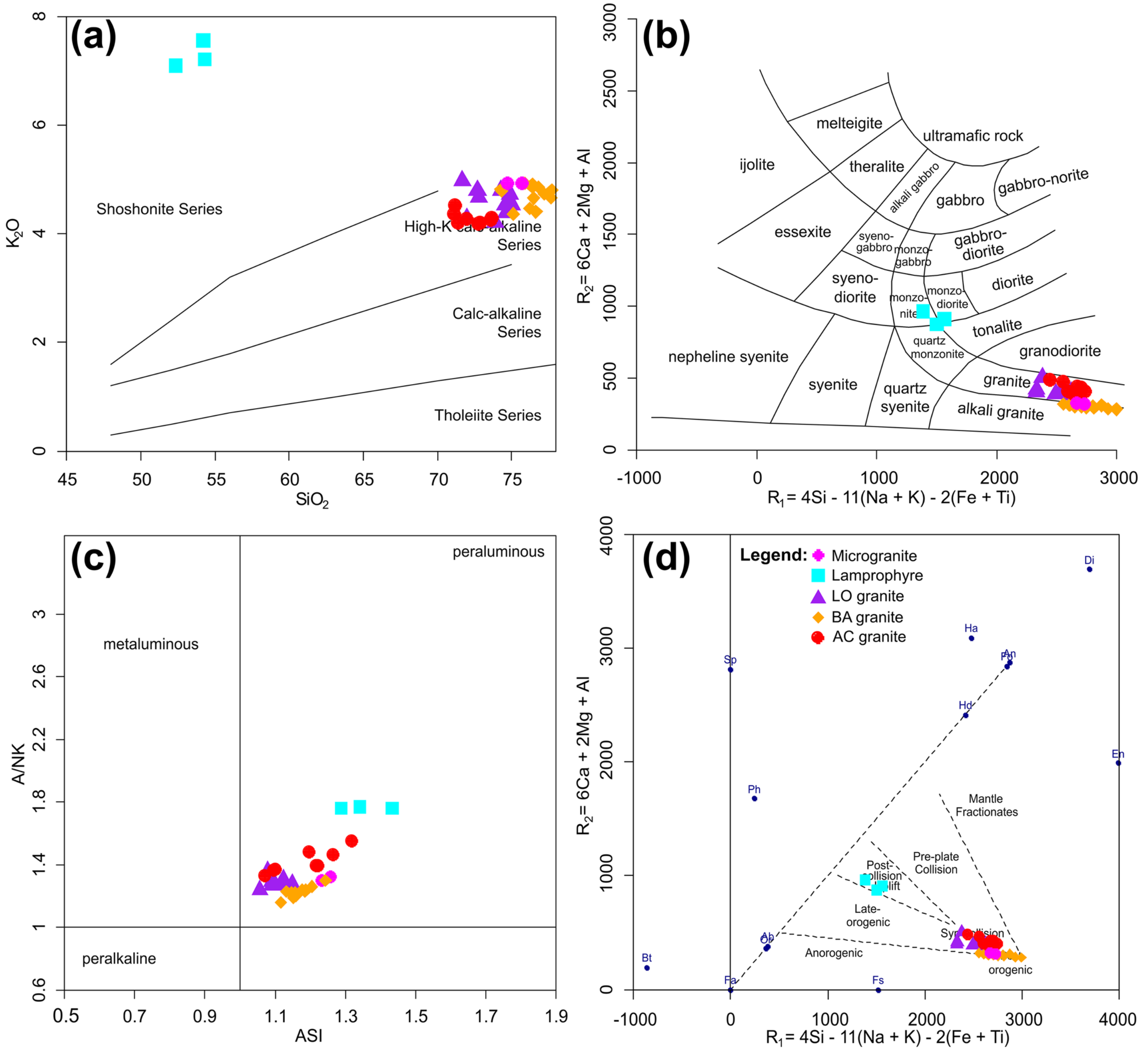

Fig. 6 Projection of the Lamas de Olo microgranite, lamprophyre, and granites in the following diagrams: **a** - SiO$_2$ vs. K$_2$O (Peccerillo & Taylor, 1976); **b** - R$_1$ vs. R$_2$ (De la Roche et al., 1980); **c** - ASI vs. A/NK (Frost et al., 2001); **d** - R$_1$ vs. R$_2$ (Batchelor & Bowden, 1985). LOP granite data after Helal (1992) and Cruz (2020)

are colorless to slightly brownish. Some crystals present a light-yellow shade while others have a few inclusions (namely melt inclusions and/or apatite, biotite, monazite, and opaques). Average uranium and thorium contents are high and widely variable (U: 138.8–6989.0 ppm; Th: 23.5–10,421.3 ppm). Common lead is low ($f^{206} < 2.3\%$) and most crystals are concordant (discordance < 10%) (Fig. 12). The Th/U ratio ranges between 0.04–2.10 (mean Th/U = 0.63), which is characteristic of primary zircon crystals in mafic or intermediate lithologies (Rubatto & Gebauer, 2000; Zeng et al., 2020). Weighted means (errors reported at one σ level) of the 204-corrected ^{206}Pb/^{238}U age yield a value of 295 ± 2 Ma (MSWD = 2.1), and presumably represent the lamprophyre crystallization age.

The Sr and Nd isotope composition of the Lamas de Olo lamprophyre yields the following results: $(^{87}Sr/^{86}Sr)_{295\ Ma} = 0.7056$; $\varepsilon Nd_{295Ma} = -0.05$; $T_{DM} = 816$ Ma; $T_{DM2} = 1022$ Ma. This data indicates that the analyzed dyke displays a composition representative of a slightly enriched mantle, similar to the Bulk Silicate Earth. The single-stage depleted mantle model age (T_{DM}) was calculated using the equation of DePaolo (1981), as

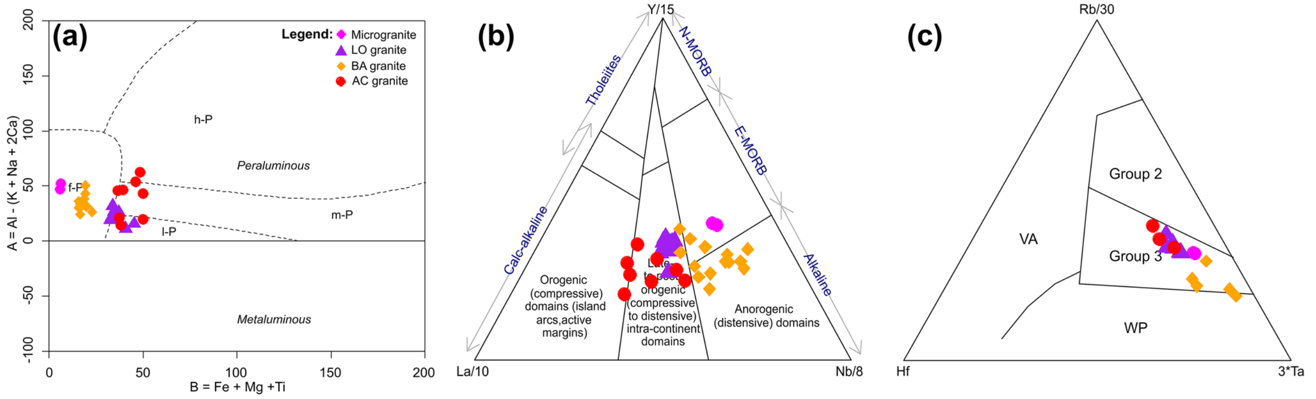

Fig. 7 Projection of the Lamas de Olo microgranite and granites in the following diagrams: **a** - B-A (Debon & LeFort, 1983; Villaseca et al., 1998); **b** - La/10-Y/15-Nb/8 (Cabanis & Lecolle, 1989); **c** - Hf-Rb/30-3Ta (Harris et al., 1986). LOP granite data after Helal (1992) and Cruz (2020). Legend: *l-P* - low-peraluminous; *m-P* - moderately peraluminous; *h-P* - highly peraluminous; *f-P* - highly felsic peraluminous; *VA* - volcanic arc; *WP* - within-plate

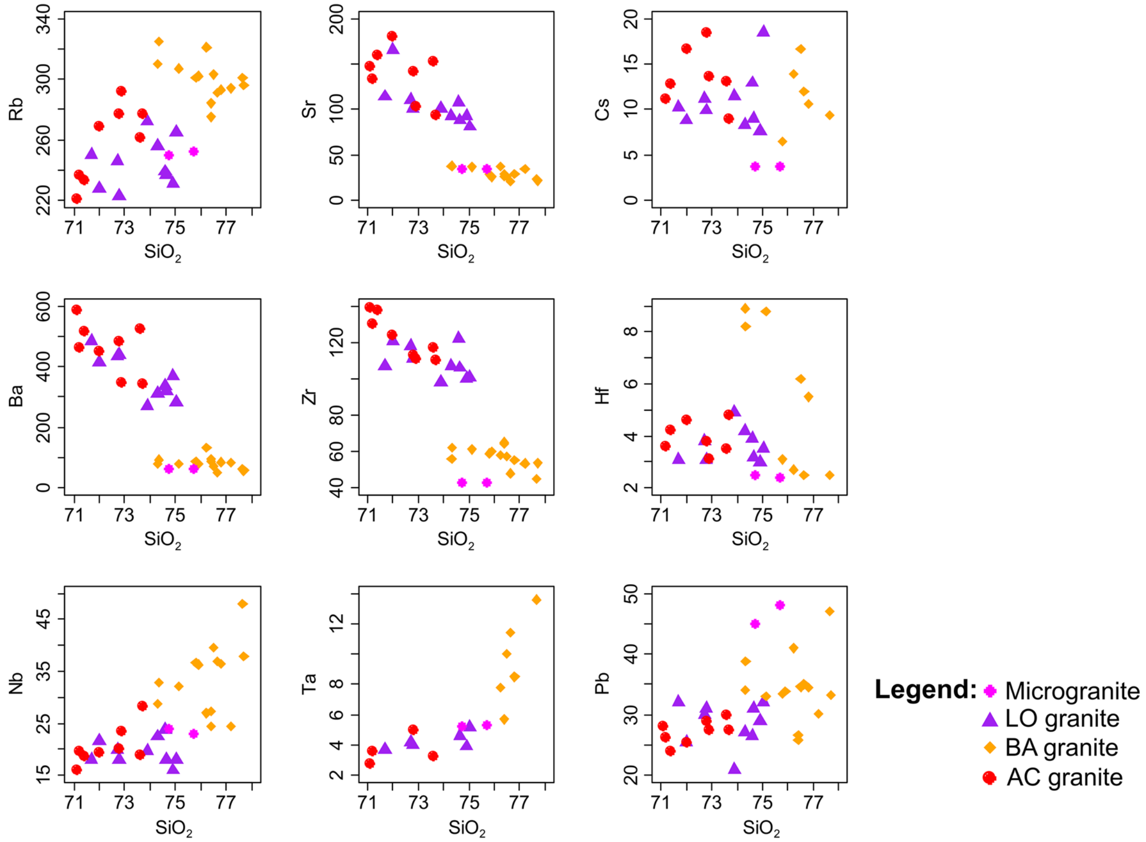

Fig. 8 Harker diagrams for trace elements of the microgranite and granitic facies of the Lamas de Olo pluton. LOP granite data after Helal (1992) and Cruz (2020)

well as the $(^{143}Nd/^{144}Nd)_{DM}$ and $(^{147}Sm/^{144}Nd)_{DM}$ ratios of Michard et al. (1985). Determination of the double-stage depleted mantle model age (T_{DM2}) was based on the equation and $(^{143}Nd/^{144}Nd)_{DM}$, $(^{147}Sm/^{144}Nd)_{DM}$, and $(^{147}Sm/^{144}Nd)_{CC}$ ratios of Liew and Hofmann (1988). Additional data are given in Online Resources 1 and 2.

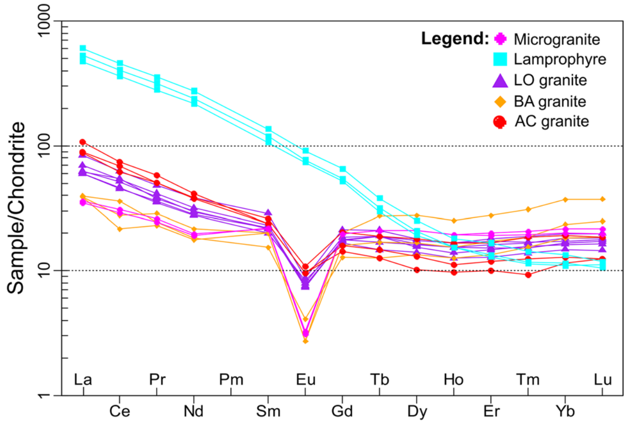

Fig. 9 REE diagrams for the Lamas de Olo microgranite, lamprophyre, and granites. Chondrite normalization values after Boynton (1984). LOP granite data after Helal (1992) and Cruz (2020)

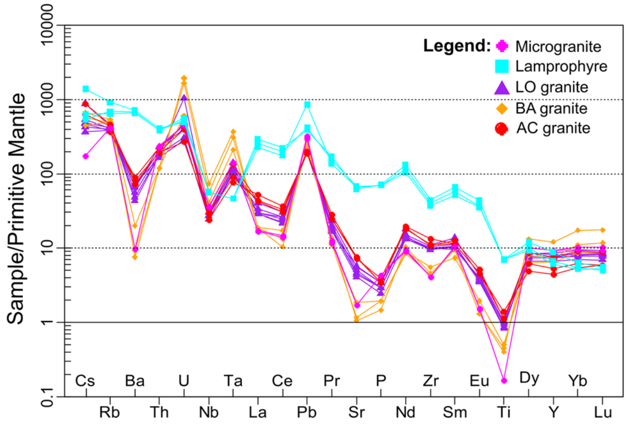

Fig. 10 Multi-element spidergrams for the Lamas de Olo microgranite, lamprophyre, and granites. Primitive mantle normalization values after McDonough and Sun (1995). LOP granite data after Helal (1992) and Cruz (2020)

5 Discussion

5.1 Petrogenesis and emplacement of the microgranite dyke

Petrographic evidence, namely feldspar kaolinization and muscovitization, as well as biotite chloritization, suggest that the Lamas de Olo microgranite was affected by post-magmatic alterations. However, since the LOI contents are lower than the typical range for highly altered rocks (LOI (Loss On Ignition) = 2–5%; Kirstein et al., 2006), the bulk-rock chemical compositions are presumably valid, and therefore can be used to withdraw petrogenetic interpretations. The absence of a significant correlation between major and minor element contents and LOI values is another argument in favor of the validity of the whole-rock analyses.

Multiple geochemical features indicate that the melt from which the microgranite was generated is more evolved than the Lamas de Olo and Alto dos Cabeços granites. These features include: (i) the lower contents in ferromagnesian elements ($Fe_2O_3^t$, TiO_2, MgO, MnO), and higher SiO_2 and K_2O contents of the microgranite; (ii) the depletion in trace elements such as Ba, Sr, Zr, and Hf; (iii) the relatively flat shape of the microgranite REE spectra; (iv) the anomalies shown by the multi-element spidergrams; and (v) the geochemical classifications as illustrated in Figs. 6a–c and 7a. The higher P_2O_5 contents of the microgranite may also be regarded as a typical characteristic of more evolved granite melts. This is because, in biotite-rich, more primitive granites, the fractionation of P-bearing minerals and influence of hydrothermal fluids generate low P_2O_5 contents (Breiter et al., 2002; Broska et al., 2004), while highly evolved granites are generally rich in phosphorus due to the higher solubility of apatite in peraluminous granitic magmas (Bea et al., 1992).

The binary diagrams for major and minor elements suggest that the microgranite could have been derived from one of the granitic pulses that generated the Lamas de Olo pluton, provided that magma evolution developed according to a continuous and undisturbed fractional crystallization of quartz, An-rich plagioclase, biotite, and Fe-Ti oxides. Such evolution would explain the downward trend in the Harker diagrams for $Fe_2O_3^t$, MgO, CaO, and TiO_2. The existence of a genetic linkage between the Lamas de Olo microgranite and pluton is also supported by similar trends in the Harker diagrams for trace elements. The depletion in barium and strontium is related to the fractionation of plagioclase (Teixeira, 2008), while the low zirconium and hafnium contents are associated with zircon fractionation.

Wu et al. (2017) stated that granites whose REE spectra reveal a flat shape are more evolved because REE contents tend to decrease as granite fractionation progresses, and the LREE/HREE ratio decreases as the Eu anomalies become more negative. Regarding the REE contents and spectra of the Lamas de Olo microgranite, the more pronounced Eu anomalies indicate that the microgranite melt was subjected to a stronger plagioclase fractionation than the pluton main pulse, while the lower REE contents suggest that the granites crystallized from magmas that underwent weak fractionations in REE-bearing minerals (namely apatite, monazite, allanite, and xenotime). On the other hand, the various anomalies identified in the multi-element spidergrams, both in High Field Strength Elements (HFSE: Th, U, Ta, Nb, Zr, REE, Hf, Ti) and Large Ion Lithophile Elements (LILE: Cs, Rb, Ba), imply that the microgranite was generated from an enriched crustal source (i.e. metapelitic; Fig. 13), which was probably uncontaminated by mantellic or young crustal influences (Nédélec & Bouchez, 2015). There is also no field or petrographic evidence suggesting an imprint of the latter

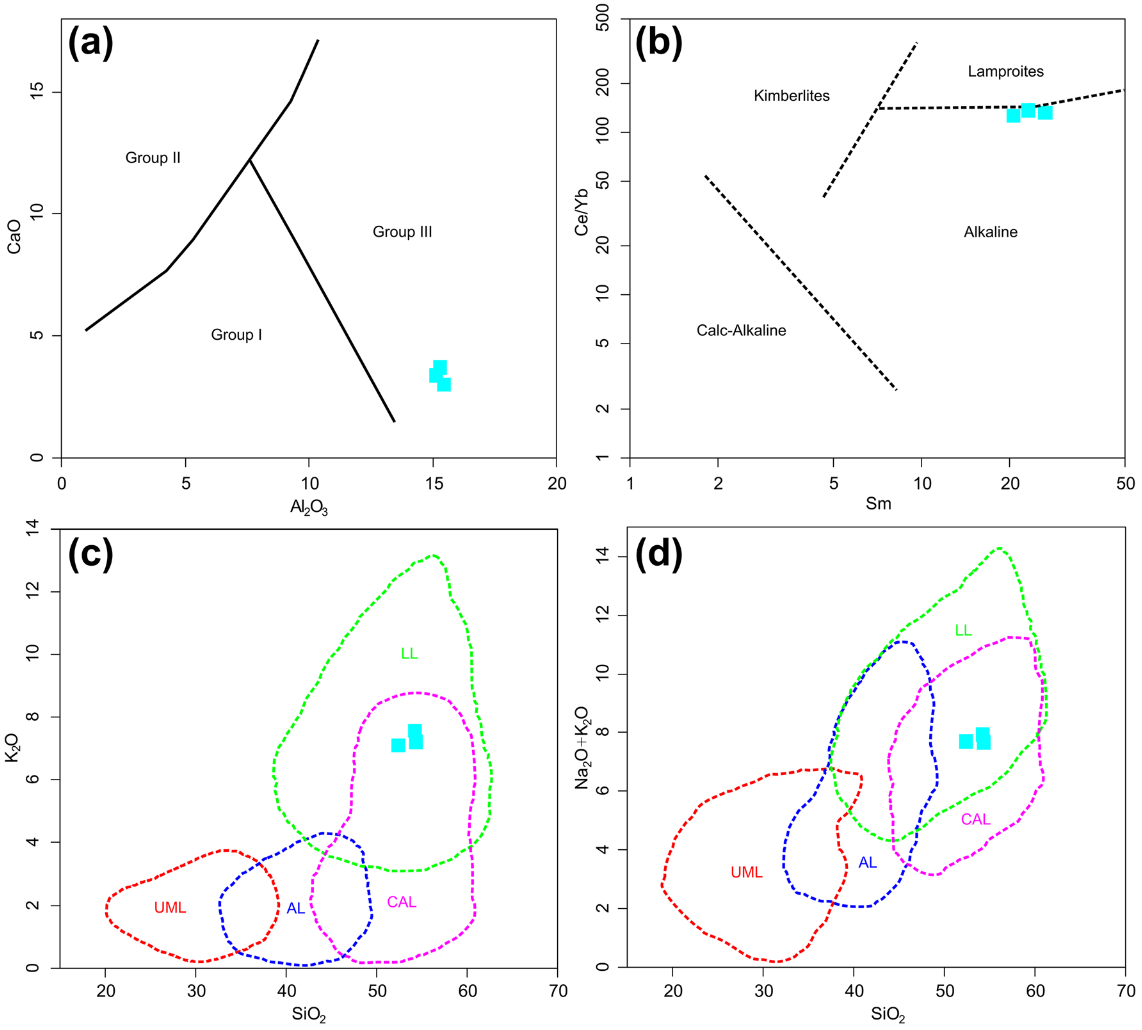

Fig. 11 Projection of the Lamas de Olo lamprophyre in the following diagrams: **a** - Al$_2$O$_3$ vs. CaO (Foley et al., 1987); **b** - Sm vs. Ce/Yb (Rock, 1991); **c** - SiO$_2$ vs. K$_2$O (Rock, 1987); **d** - SiO$_2$ vs. Na$_2$O + K$_2$O (Rock, 1987). Legend: *UML* - ultramafic lamprophyres; *AL* - alkaline lamprophyres; *CAL* - calc-alkaline lamprophyres; *LL* - lamproites

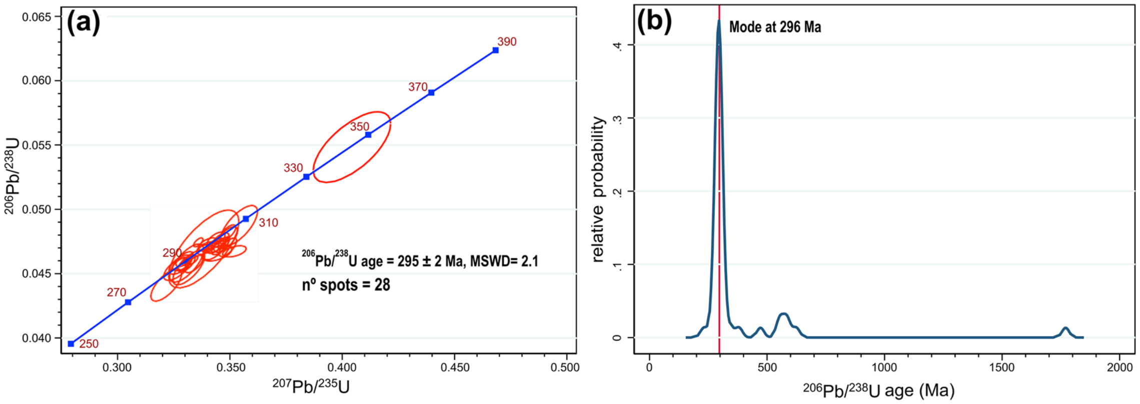

Fig. 12 **a:** Wetherill concordia plot for the Lamas de Olo lamprophyre; **b:** relative probability distribution of crystallization ages

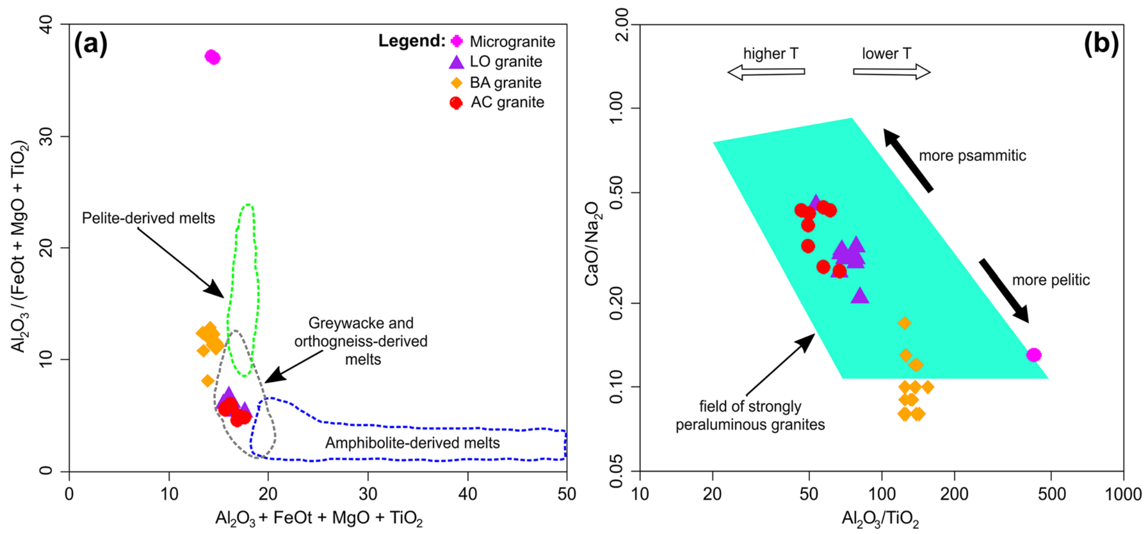

Fig. 13 Projection of the Lamas de Olo microgranite and granites in the following diagrams: **a** - $Al_2O_3 + FeO^t + MgO + TiO_2$ vs. $Al_2O_3/(FeO^t + MgO + TiO_2)$ (fields of experimentally determined pelite-derived, greywacke and orthogneiss-derived, and amphibolite-derived melts after Patiño Douce (1999) and Jung et al. (2009)); **b** - Al_2O_3/TiO_2 vs. CaO/Na_2O (field of strongly peraluminous granites after Sylvester (1998)). LOP granite data after Helal (1992) and Cruz (2020)

influences. In the spidergrams, the notable positive anomaly in lead constitutes another argument in favor of the highly evolved nature of the microgranite melt (Finger & Schiller, 2012).

The overall whole-rock geochemistry of the microgranite and Barragem granite are identical, as evidenced by the similar compositions concerning major, minor, and trace elements (including REE), the parallelism of the REE spectra and multi-element spidergrams, and the matching classifications. Altogether, this data implies a stronger genetic association between these two lithologies, as well as a higher evolutionary degree. As such, it is reasonable to presume that the microgranite possibly derived from the same source that generated the Barragem facies. Even though both rocks are plotted on the post-orogenic fields of the Batchelor and Bowden (1985) and Harris et al. (1986) diagrams, the magnesian nature (Frost et al., 2001) and anorogenic signature (Cabanis & Lecolle, 1989) point to a more transitional character. Given this newly established relationship, the bulk-rock geochemistry also suggests that the microgranite is younger than the Lamas de Olo and Alto dos Cabeços granites.

According to Oliveira et al. (2019), the magnetic fabric of the Lamas de Olo felsic dyke is undefined since the average magnetic lineation (7°/N62°E) and average magnetic foliation (N43°E–19°SE) are both oblique regarding the E-W main trend. Such results imply the occurrence of severe post-magmatic alterations on the magnetic (and ferromagnesian) minerals (Hrouda, 1985; Raposo, 2011), which would explain the significant differences between the microgranite and Barragem granite in Fig. 13a. As previously mentioned, the microgranite has in fact been altered, which is mainly evidenced by the petrographic results. However, what remains to be analyzed is whether these alterations were caused by hydrothermal or meteoric fluids. Ballouard et al. (2016) suggested the use of the Nb/Ta ratio to evaluate the magmatic-hydrothermal transition in granitic rocks rather than the K/Rb ratio since the latter is based on more mobile elements (LILE). Nonetheless, both ratios can be used in conjunction to evaluate the influence of hydrothermal fluids. Hydrothermally-altered granites typically show $Nb/Ta < 5$ and $K/Rb < 150$. The microgranite exhibits $Nb/Ta = 4.34–4.62$ and $K/Rb = 162.34–163.64$. As such, it is plausible to assume that even though the microgranite was affected by hydrothermal alterations, these were not significant, and thus, the magnetic fabric was essentially influenced by meteoric fluids. The weak phosphorus anomaly registered in the multi-element spidergrams corroborates the low degree of hydrothermalism.

Given the general orientation of the dyke and the likely relationship with the pluton, the emplacement of the Lamas de Olo microgranite was most likely controlled by the WSW–ENE trending fracture system. Even though the melt that originated the Barragem granite presumably ascended through a different fault system (NNE–SSW), pluton emplacement and ascent were conditioned by the intersection of all three regional fracture systems (Cruz, 2020), meaning that a small portion of magma, similar to the one from which the BA facies was derived (i.e. the microgranite), could have ascended along a different, albeit spatially close, structure.

The differences between the microgranite and Barragem granite mainly concern texture. However, these can easily be explained by the field relations and thermal contrasts at the time of emplacement. Whole-rock geochemistry and geological contacts suggest that both the BA granite and microgranite are younger than the remaining facies of the pluton. Since all granites are post-tectonic, during the emplacement of the Barragem facies, the corresponding melt intruded into the host Lamas de Olo facies which was clearly warmer than the surrounding host metasedimentary rocks and syntectonic granites. On the other hand, the microgranite magma emplaced into the colder, syntectonic granites, resulting in a finer granularity and less phaneritic texture. It is also likely that the tabular shape of the intrusion and small thickness of the dyke further contributed to the development of the microphaneritic texture. The greater thermal contrast between the microgranite melt and respective host rocks is also recorded by small fractures appearing in the microgranite near the contact. These fractures were filled by veinlets, whose granularity is coarser than that of the felsic dyke. The veinlets are possibly cogenetic with the microgranite and represent a final magmatic segregation. Since the microgranite melt was emplaced as a dyke, rapid heat transfer, cooling, and volatile loss are likely to have occurred. The abundant micrographic and granophyric intergrowths also suggest that the cooling rates and undercooling magnitude of the melt were variable (Štemprok et al., 2008). On the other hand, the presence of magmatic to submagmatic microstructures in quartz (incipient undulatory extinction and rare polygranular aggregates) and muscovite (cleavage bending) (Bouchez et al., 1992) is a testimony to the passive emplacement of the microgranite, since these microstructures were probably formed under the influence of a magmatic to submagmatic flow.

5.2 Lamprophyre petrogenesis and source composition

Taking into account the findings of Scarrow et al. (2008), the Lamas de Olo mafic dyke is a calc-alkaline to alkaline lamprophyre (Fig. 11) which, according to Rock (1991), are equivalent to volatile-rich basalts, having resulted from partial melting of hydrous mantle sources, enriched in incompatible trace elements. The alkaline signature is reflected in the high vanadium contents and low Ti/V ratios (60.0–61.9) (Štemprok et al., 2014). Even though the LOI values of the studied lamprophyre range between 3.92–4.25%, they might not reflect the post-magmatic alterations that have affected this lithology. The reason for this is because Rock (1991) argued that the high LOI values of lamprophyres are a primary attribute that is directly related to the characteristic high H_2O and CO_2 contents. Moreover, deuteric alterations in lamprophyres could be the result of autometasomatic processes caused by volatile exsolution (Rock, 1991). Nonetheless, petrographically, there is ample evidence for the effects of post-magmatic alterations such as feldspar kaolinization,

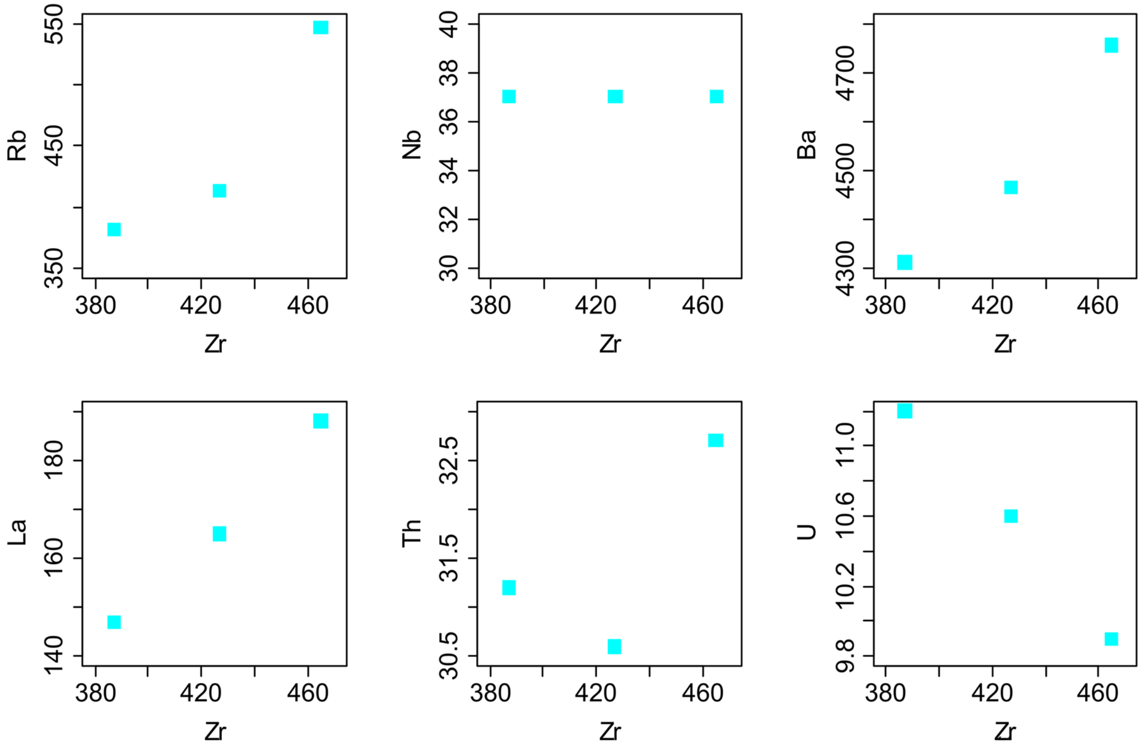

Fig. 14 Binary diagrams for Zr vs. Rb, Nb, Ba, La, Th, and U of the Lamas de Olo lamprophyre

pyroxene uralitization, amphibole biotitization, and biotite chloritization. When compared to other Variscan lamprophyres (Štemprok et al., 2014), the Lamas de Olo specimen is depleted in Na_2O and CaO, which is presumably due to the fluid-promoted feldspar alteration (Förster et al., 2007).

Previous studies (Oliveira et al., 2019) have shown that the magnetic fabric of this lamprophyre is near-type III (Hrouda et al., 2016) because while the average magnetic lineation is subperpendicular to the dyke trend (40°/N138°E), the average magnetic foliation is oblique (N105°E–57°SW). Such magnetic fabrics have been typically attributed to post-magmatic processes (Raposo & Ernesto, 1995). Nevertheless, since several incompatible trace elements (e.g. Rb, Nb, Ba, REE, Th) are strongly correlated with zirconium (Fig. 14), which is highly immobile when faced with low to medium-grade metasomatic and hydrothermal phenomena (Inglis et al., 2018; Liu et al., 2020), post-magmatic influences on the Lamas de Olo lamprophyre were only moderately significant.

The only evident relationship between the Lamas de Olo pluton and lamprophyre is structural since, considering the dyke trend, the NNE–SSW fracture system associated with the LOP possibly played an important role in the lamprophyric magma emplacement. As explained in the previous subchapter, the intersection of all regional fault systems is suggested to have controlled the emplacement of the pluton (Cruz, 2020). As such, even though the NNE–SSW fractures mainly conditioned the petrophysics of the Barragem granite, other melts could have also ascended along this fault system. On the other hand, several microstructures, such as the kinks and cleavage bending on biotite phenocrysts, as well as the weak undulatory extinction on quartz crystals, which were probably generated through the influence of a magmatic to submagmatic flow (Bouchez et al., 1992), highlight the passive emplacement of the lamprophyre. Other textural features (namely the corrosion gulfs, skeletal texture, and reaction rims around quartz xenocrysts) can be explained through rapid heat transfer and volatile loss (Štemprok et al., 2008). The latter processes were probably caused by a fast ascent of the lamprophyric melt which is typical for igneous rocks occurring as dykes (Vernon, 2004).

As previously mentioned, the magma that generated the Lamas de Olo lamprophyre was not primitive. This fact is not only evidenced by the intermediate to basic character and low MgO contents, but also by the low Cr (230–250 ppm) and Ni concentrations (70–90 ppm) since primitive melts that derived from mantle sources show Cr > 500–1000 ppm and Ni > 200–500 ppm (Frey et al., 1978; Wilson, 1989). Thus, it is plausible to assume that the evolution of the lamprophyric magma was partially conditioned by fractional crystallization. However, other scenarios, such as crustal contamination, could account for the non-primitive features of the mafic dyke. Ratios of trace elements whose contents in the mantle and crust are significantly different can be used to assess possible contaminations and/or metasomatic enrichment of the mantle source (*e.g.* Perini et al., 2004, Kirstein et al., 2006; Orejana et al., 2008; Ma et al., 2014; Soder & Romer, 2018; Liu et al., 2020). Taking into account the geochemistry of the Lamas de Olo lamprophyre, there is ample evidence for such inputs, namely the following: (i) enrichment in Ba, Th, U, and LREE; (ii) negative anomalies in Nb and Ta; (iii) high Ba/Nb ratios (117–129), which also reflect the strong alkaline signature; (iv) high La/Ta ratios (86.5–110.6); (v) low Y/Nb ratios (0.7–1.0); (vi) low Nb/U ratios (3.3–3.7); (vii) low Ce/Pb ratios (2.3–6.4); and (viii) lack of correlation between Zr and U contents (Fig. 14). The strong positive anomalies in alkali metals (Rb and Cs) can be regarded as another argument for these influences. The problem is that both assimilation and mantle metasomatism triggered by subduction-related fluids and/or melts can generate mantle sources with crust-like trace element signatures. Thus, at this point, neither phenomena can be excluded for consideration regarding the petrogenetic evolution of the Lamas de Olo lamprophyre.

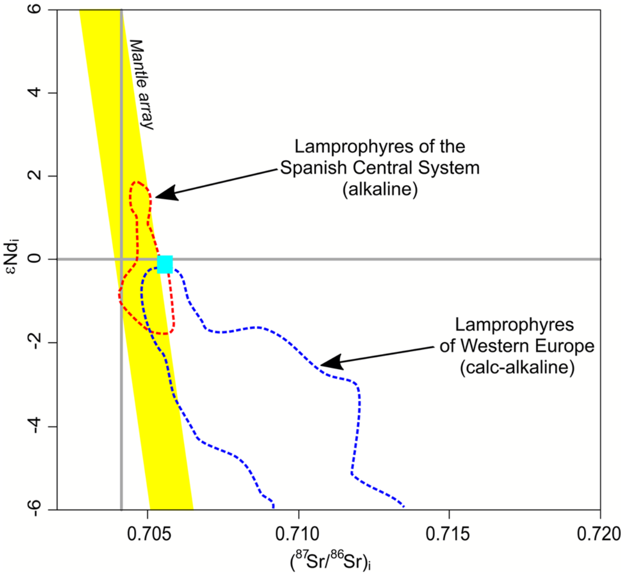

Fig. 15 Projection of the Lamas de Olo lamprophyre in the $(^{87}Sr/^{86}Sr)_i$ vs. εNd_i plot. The fields of lamprophyres from the Spanish Central System and Western Europe were taken from Orejana et al. (2020) and Soder and Romer (2018), respectively. Mantle array after Wilson (1989)

In a recent study, Bea et al. (2021) proposed new theories to explain the generation of other potassic basic to intermediate rocks in Central Iberia, namely appinites and vaugnerites. Based on the bulk-rock and isotope compositions, the authors consider that these lithologies resulted from mixing of mantellic and crustal magmas, generated near the crust-mantle boundary. While the appinites were presumably exposed to further contamination as the corresponding

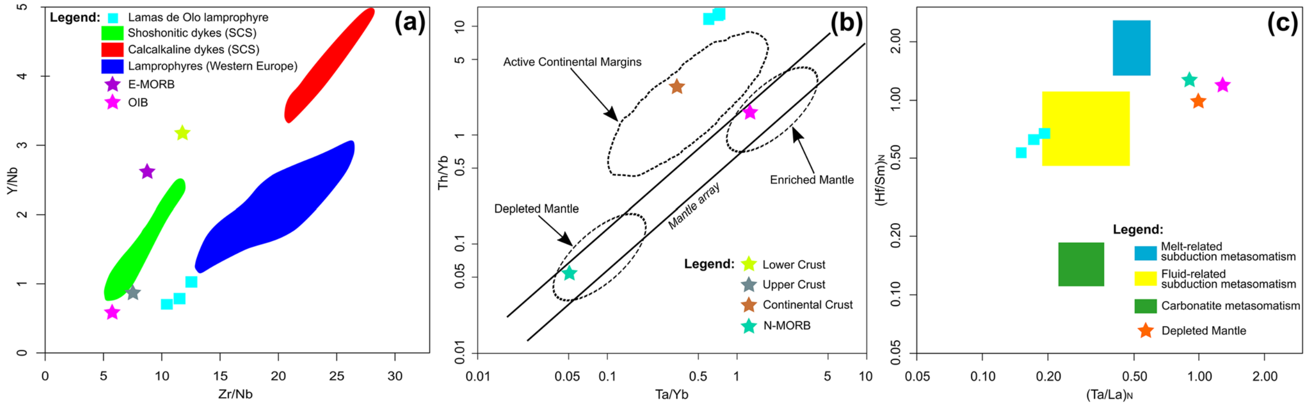

Fig. 16 Projection of the Lamas de Olo lamprophyre in the following diagrams: **a** - Zr/Nb vs. Y/Nb (fields of rocks from the Spanish Central System and Western Europe after Perini et al. (2004) and references therein); **b** - Ta/Yb vs. Th/Yb (the field depicting active continental margins was taken from Wilson, 1989); **c** - $(Ta/La)_N$ vs. $(Hf/Sm)_N$ (fields representing distinct metasomatic components taken from LaFlèche et al. (1998) and references therein). Average OIB, E-MORB, N-MORB, Depleted Mantle, and Enriched Mantle compositions after Sun and McDonough (1989). Average lower and upper crust compositions after Rudnick and Fountain (1995). Average continental crust composition after Rudnick and Gao (2003)

melts intruded through fertile crustal rocks, the vaugnerites possibly became enriched due to supercritical fluids released from biotite breakdown. Considering the isotope signatures, these hypotheses are probably not suited to explain the petrogenetic evolution of the Lamas de Olo lamprophyre, as the appinites and vaugnerites of Central Iberia are, in general, more radiogenic ($\varepsilon Nd_i = -2$ to -6; $(^{87}Sr/^{86}Sr)_i > 0.706$; Bea et al., 2021). What is clear from the isotope data is that the studied specimen is identical when compared to other late to post-Variscan lamprophyres of the CIZ and Western Europe (Fig. 15). Since most of these lamprophyres present either only minor or no evidence of crustal contamination (*e.g.* Bea et al., 1999; Orejana et al., 2008; Ubide et al., 2010; Scarrow et al., 2011; Štemprok et al., 2014; Soder & Romer, 2018; Orejana et al., 2020), the same can be assumed for the Lamas de Olo mafic dyke. The high Sr and REE contents support this theory (Ma et al., 2014). Furthermore, Orejana et al. (2008) suggested that contaminations caused by silica-rich rocks can be proved through positive correlations between SiO_2 and the Rb/Sr ratio. Despite the low number of samples, the previous ratio and SiO_2 contents are not correlated (not shown) which constitutes another argument for the insignificant role of crustal contamination. However, the influence of the latter process should not be completely ruled out, as the presence of quartz xenocrysts is probably related to contamination.

From the last two paragraphs, three ideas have been made clear: (i) the Lamas de Olo lamprophyre is compositionally similar to many other European lamprophyres generated during the final stages of the Variscan orogeny (as evidenced in Figs. 15 and 16a); (ii) crustal contamination has, most likely, played only a minor role in the petrogenesis; and (iii) the crust-like trace element signatures are possibly related to metasomatism in the source, thus explaining the enriched nature and position of the studied dyke in Fig. 16b. On the other hand, the occurrence of fractional crystallization is registered in the near-constant Th/Nb, Th/Hf, La/Sm, La/Yb, and Ce/Yb ratios: 0.83–0.88, 3.03–3.30, 7.07–7.11, 63.9–68.8; 127.4–137.1, respectively (Allègre & Minster, 1978; Kirstein et al., 2006; Liu et al., 2020). By resorting to the composition of primitive and compositionally identical late-Variscan lamprophyre magmas (minettes) taken from the literature, an approximation to the mineral fractionation can be reasonably made. The data used for this purpose was withdrawn from Štemprok et al. (2014), Errandonea-Martin et al. (2018), and Soder and Romer (2018). As illustrated in Figs. 17a and b, Cr and Ni are positively correlated with MgO, which suggests the fractional crystallization of mafic minerals such as olivine, spinel, and clinopyroxene. On the other hand, the approximately constant CaO/Al_2O_3 ratio (0.19–0.24) along with the positive correlation between CaO and MgO (Fig. 17c), and the correlated $Fe_2O_3{}^t$, TiO_2, and MgO contents (Fig. 17d and e) respectively point out the fractional crystallization of amphibole and Fe-Ti oxides. Also, the Y/Nb ratio and P_2O_5 contents display a negative correlation (Fig. 17f), which may be due to an accumulation of apatite (Perini et al., 2004). Considering the absence of Eu anomalies on the REE spectra and the lack of correlations between Na_2O and Al_2O_3 with MgO (Fig. 17g and h), plagioclase fractionation did not occur.

As previously observed, the lamprophyre is richer in LREE over HREE which could be due to the crystallization of HREE-bearing minerals from the lamprophyric melt. Also, the REE spectra are highly fractionated. This information, along with the anomalies revealed by the multi-element spectra, suggests that the mafic dyke derived

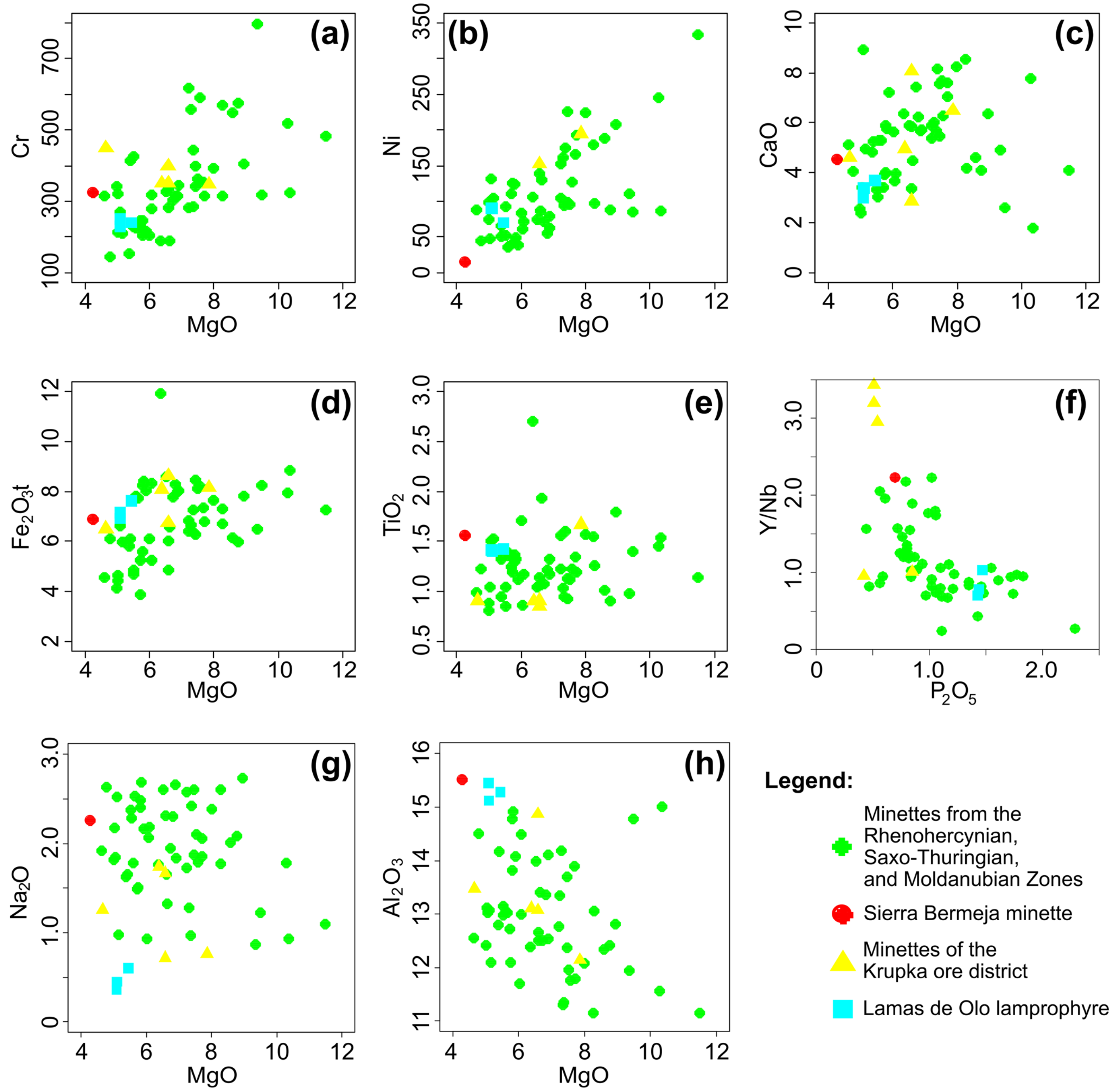

Fig. 17 Binary diagrams for: **a** - MgO vs. Cr; **b** - MgO vs. Ni; **c** - MgO vs. CaO; **d** - MgO vs. $Fe_2O_3^t$; **e** - MgO vs. TiO_2; **f** - P_2O_5 vs. Y/Nb; **g** - MgO vs. Na_2O; and **h** - MgO vs. Al_2O_3 of the Lamas de Olo lamprophyre and other late to post-Variscan minettes. Sources: Minettes of the Rhenohercynian, Saxo-Thuringian, and Moldanubian Zones (Soder & Romer, 2018); Sierra Bermeja specimen (Errandonea-Martin et al., 2018); Minettes of the Krupka ore district (Štemprok et al., 2014)

from a deep-seated, REE-enriched mantle source. On the other hand, the low Nb/La ratios (0.20–0.25) indicate that the source was probably located on the lithospheric mantle since this reservoir is depleted in HFSE (such as Nb) in regard to LREE (Bayat & Torabi, 2011). As explained in the previous paragraphs, many geochemical features also highlight the enriched character of the mantle source, namely: (i) the Sr and Nd isotope signatures; (ii) the low Zr/Nb ratio (10.5–12.6); (iii) the moderate V/Cr ratio (0.56–0.59); and (iv) the high Th/Ce ratio (0.09–0.11). Since the multi-element spidergrams present strong positive anomalies in LILE (K and Rb) and Pb, as well as negative anomalies in HFSE (Nb, Ta, Zr, Hf, Ti), subduction-related materials are likely to be responsible for the mantle source enrichment. The influence of a previous subduction event is reflected in several trace element ratios such as Ta/Yb (0.6–0.7), the low Lu/Hf (≈ 0.03), Sm/Nd (≈ 0.16), and Sm/La (≈ 0.14), the high Th/La (0.17–0.21), La/Nb (4.0–5.1), and Th/Ta (18.0–19.2), as well as the Th/Yb ratio (11.7–13.6) whose values are higher than those of N-MORB (Zeng et al., 2020). European lamprophyres of late-Variscan age typically present high contents in Rb, Ba, Pb, Sr, U, and Th, high values for the Th/La ratio, and low values for the Sm/La ratio (Štemprok et al., 2014 and references therein). Based on the analytical results reported in this paper, the Lamas de Olo lamprophyre is no exception. Also, it has been suggested that all of the previous features resulted either from contributions of the continental crust, or metasomatism triggered by aqueous fluids or hydrous melts that were related to the subducted crust and associated sediments (Štemprok et al., 2014 and references therein). Based on the (Ta/La)$_N$ vs (Hf/Sm)$_N$ diagram (after LaFlèche et al., 1998; Fig. 16c), fluid-related subduction metasomatism is likely to have occurred. Considering the high Eu/Ti and Zr/Hf ratios (6.46–7.85 and 39.9–46.9, respectively), and the presence of magnetite and apatite, the metasomatic event might have been caused by carbonate-rich fluids (Bayat & Torabi, 2011). The latter hypothesis is supported by the findings of Shaw et al. (2003) and Dasgupta et al. (2004) which respectively demonstrated that the transport of carbonate minerals by subduction into the mantle and their survival in the deep subduction geotherm are possible.

Other important information that trace element ratios may provide concerns the type of residual phases that dwelled in the mantle sources. The low values for the Rb/Ba and Rb/Sr ratios (0.09–0.12 and 0.29–0.44, respectively) suggest that the source of the Lamas de Olo lamprophyre was richer in residual amphibole over phlogopite (*e.g.* Bayat & Torabi, 2011). This is because phlogopite preferentially incorporates LILE over HFSE and REE (Orejana et al., 2008). Considering the Nb/Ta ratio (≈ 21.8), the residual amphibole was probably pargasite (Green, 1995). However, since the Rb/Sr ratios are higher than 0.1 and Ba/Rb ratios are lower than 20 (8.7–11.3), phlogopite is likely to have also been present in the mantle source (Furman & Graham, 1999). On the other hand, the values of the Th/La and Sm/La ratios, as well as the high Th/U ratios (2.8–3.3) point out the presence of LREE-bearing residual phases, namely allanite, in the subducted continental crust component. Phengite might have also existed as a residual phase in the latter component because the K$_2$O/Na$_2$O ratios are very high (Soder & Romer, 2018).

The remarkable general REE fractionation of the Lamas de Olo mafic dyke not only suggests the presence of garnet in the source but also supports the existence of residual allanite (LREE-rich) and amphibole (MREE-rich). Since the values concerning the Dy/Yb ratio (2.7–2.9) are higher than 2.5, spinel might have also been present (Duggen et al., 2005). In Fig. 18a, the Sm/Yb ratio is plotted against Sm contents, while in Fig. 18b the former ratio is plotted against a different one (La/Yb). Alici Şen et al. (2004) stated that the Sm/Yb ratio varies according to the proportion of garnet in the source. Thus, it can be used to pinpoint the source mineralogy of mantle-derived igneous rocks (since HREE are compatible with garnet). Considering the results, the source of the Lamas de Olo lamprophyre is likely to have been garnet and spinel-bearing (as opposed to what has been verified for the Spanish specimens which are suggested of being

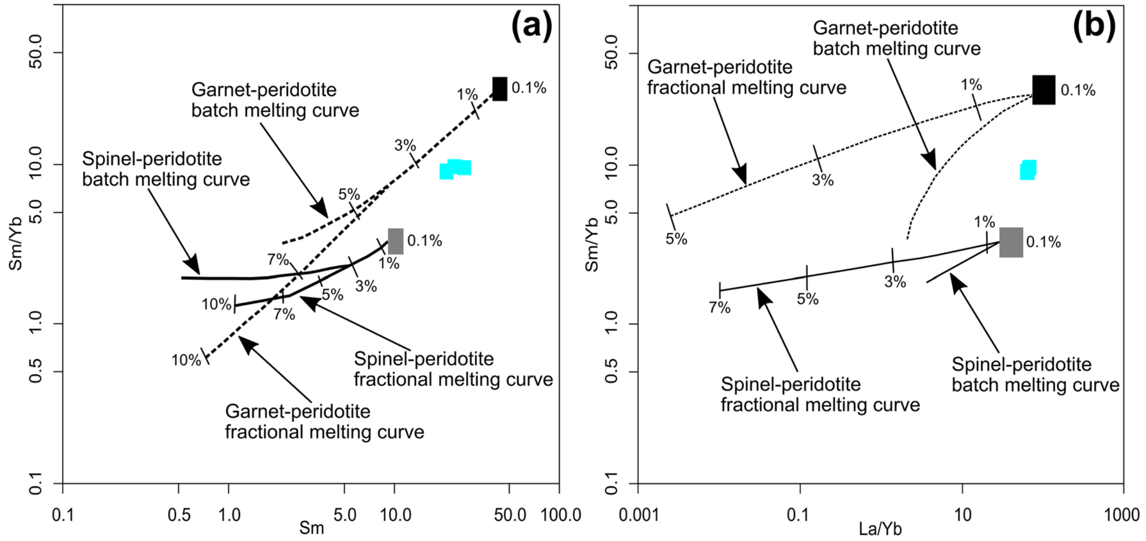

Fig. 18 Projection of the Lamas de Olo lamprophyre in the: **a** - Sm vs. Sm/Yb; and **b** - La/Yb vs. Sm/Yb diagrams (Alici Şen et al., 2004). The black and grey fields respectively represent the starting compositions of garnet and spinel-bearing peridotites at a 0.1% melting degree. Melting curves were obtained from the equations of Shaw (1970). Garnet and spinel peridotite compositions are from Sen and Leeman (1991) and McDonough (1990).

mostly derived from garnet-bearing sources (*e.g.* Orejana et al., 2020)). Similar observations have been pointed out by Ma et al. (2014). The fact that the samples for this dyke are displaced to the right of both the garnet-peridotite and spinel-peridotite batch melting curves constitutes further evidence of the enriched nature of the mantle source (Kirstein et al., 2006). Also, these diagrams clearly indicate that the lamprophyric melt possibly resulted from low-degree melting of the source.

5.3 Lamas de Olo in the Permo-Carboniferous magmatism setting

Most studies about the petrogenesis of lamprophyres in the Spanish Central System advocate that lithosphere thinning, passive upwelling of asthenosphere-derived mantle magmas, and melting triggered by adiabatic decompression is the most feasible geodynamic scenario (e.g. Bea et al., 1999; Orejana et al., 2008; Scarrow et al., 2011). Even though a few lamprophyres from the Spanish section of the Central Iberian Zone have been classified as minettes or kersantites (Errandonea-Martin et al., 2018), most of them are camptonites, i.e. alkaline lamprophyres sensu *strictu* (Rock, 1991). On the other hand, calc-alkaline Variscan lamprophyres from the Moldanubian, Saxo-Thuringian, and Rhenohercynian Zones are associated with more orogenic settings, and their mantle sources are suggested to have been affected by subduction-related materials and metasomatism (Soder & Romer, 2018; Štemprok et al., 2014). Taking into account the bulk-rock composition, isotope geochemistry, and geochronological results, the Lamas de Olo lamprophyre shares more resemblances with the calc-alkaline specimens (Figs. 15 and 16a). The greater similarity with late-Variscan lamprophyres of the Moldanubian and Saxo-Thuringian Zones is also marked by the enrichment in critical metals such as Li, Sn, and W which are considered to be related to the variable degree of metasomatism that affected the mantle sources (Štemprok et al., 2014).

The geochemical signature of the studied mafic dyke is seemingly associated with orogenic processes. This is mainly evidenced by the geotectonic classification diagrams (Figs. 6d and 11), Nb contents in the range of 10–45 ppm (Semiz et al., 2012), and the Al_2O_3/TiO_2 ratio (10.74–10.93) (Müller et al., 1992). Scarrow et al. (2006) suggested that, in late-orogenic settings, K-rich mafic magmatism is commonly associated with the main collisional event, representing a final release of melts from metasomatized lithospheric mantle sources. These authors also propose that the late to post-Variscan lamprophyres may be regarded as a geodynamic pointer for a change in the tectonic regime (from extension to transtension). The previous interpretations have been corroborated by Scarrow et al. (2011) who noted that, in Europe, late-Variscan lamprophyres are typically related to local strike-slip systems that were created by the orogenic process. Based on the results presented in this paper, the case of the Lamas de Olo lamprophyre proves to be no exception, as its emplacement, textures, and microstructures were controlled by fractures generated during phase D_3 of the Variscan orogeny.

Overall, the geochemical and geotectonic classifications of the Lamas de Olo lamprophyre dyke point out a transitional to anorogenic setting, with a clear orogenic imprint. Considering the U–Pb analyses of the LO granite (Fernandes et al., 2013), the bulk-rock chemistry of the microgranite, and the geochronological results of the lamprophyre, the plutonic and subvolcanic magmatism in the Lamas de Olo region were seemingly contemporaneous. The latter observation is in agreeance with previous studies about the Permo-Carboniferous, late to post-Variscan hypabyssal magmatic event.

6 Final Remarks

The microgranite and lamprophyre dykes of the Lamas de Olo region in northern Portugal constitute a local representative of the bimodal, mainly mafic, calc-alkaline to alkaline, Permo-Carboniferous hypabyssal magmatism that is related to the late to post-orogenic stages of the Variscan cycle. Taking into account their field relations, petrography, textures, microstructures, bulk-rock and isotope geochemistry, as well as geochronological results, the following conclusions have been formulated:

1. When compared to the granitic facies that compose the Lamas de Olo pluton, the microgranite is unequivocally more evolved than the Lamas de Olo and Alto dos Cabeços granites, as implied by several data concerning the whole-rock geochemistry. The anomalies shown by the multi-element spidergrams suggest that the microgranite was derived from a metapelitic crustal source, which was probably uncontaminated by mantellic or young crustal influences. Given the great geochemical similarities between the microgranite and Barragem granite, the two lithologies possibly derived from the same source which would explain the apparent trends revealed by several Harker diagrams. Since the Barragem facies is the youngest of the pluton, the bulk-rock geochemistry also suggests that the microgranite is younger than the Lamas de Olo and Alto dos Cabeços granites. Petrographic results and previous petrophysical studies have proved that the microgranite was affected by post-magmatic alterations. Based on the Nb/Ta and K/Rb ratios, these alterations were mainly triggered by meteoric fluids. Any influence from hydrothermal processes was minimal. Considering the general orientation of the

dyke and the probable relationship with the pluton, the emplacement of the Lamas de Olo microgranite was most likely controlled by the regional WSW–ENE trending fracture system. The main differences between the Lamas de Olo microgranite and Barragem granite concern texture and microstructures. The greater thermal contrast between the microgranite melt and respective host rocks, the tabular shape of the intrusion, and the small thickness of the dyke are responsible for the finer granularity and less phaneritic texture. On the other hand, the micrographic and granophyric intergrowths are related to rapid heat transfer, cooling, and volatile loss, while the magmatic to submagmatic microstructures are a testimony to the passive emplacement of the microgranite melt.

2. The effects of post-magmatic alterations were more significant on the lamprophyre dyke, as evidenced by the petrography and bulk-rock composition. Previous petrophysical analyses have shown that deuteric alterations are the likeliest cause. There is no geochemical evidence for the existence of any sort of genetic relationship between the Lamas de Olo lamprophyre and pluton. The only connection is structural since the NNE–SSW fracture system associated with the pluton possibly played an important role in the lamprophyric magma emplacement. The melt that generated the lamprophyre was not primitive and is suggested to have been conditioned by fractional crystallization. Crustal contamination probably played only a minor role in the petrogenetic evolution. Several trace element ratios suggest that the lamprophyre was derived from an enriched mantle source, with crust-like trace element signatures, located in the lithospheric mantle. Source enrichment was presumably caused by subduction-related materials and metasomatism triggered by carbonate-rich fluids. Residual mineral phases such as pargasitic amphibole and phlogopite are likely to have been present in the lamprophyre source. Allanite and phengite, on the other hand, might have existed as residual phases in the subducted crust component. Trace elements, including REE, also indicate that the lamprophyre melt resulted from low-degree melting of the source, which was seemingly garnet and spinel-bearing.
3. When compared to other late-Variscan lamprophyres, the Lamas de Olo mafic dyke shares more similarities with the calc-alkaline specimens of Western Europe. This contemplation suggests that even though the studied lamprophyre is partially alkaline, the petrogenesis was clearly influenced by a strong orogenic signature. The present work corroborates previous studies regarding the observation that late to post-Variscan lamprophyres may constitute a geodynamic pointer for a change in the tectonic regime. Our results, along with prior works about the Lamas de Olo pluton, suggest that the regional subvolcanic and plutonic magmatic activities were coeval.

Supplementary Information The online version contains supplementary material available at https://doi.org/10.1007/s41513-021-00179-8.

Acknowledgements This work was supported by the Portuguese Foundation for Science and Technology (FCT), through the project ref. UIDB/04683/2020 - ICT (Institute of Earth Sciences). The corresponding author is financially supported by FCT through an individual Ph.D. grant (reference SFRH/BD/138818/2018). The authors thank José Carlos Oliveira and Dr. Cláudia Cruz for their help during the field studies and sample collection. We also acknowledge Dr. Javier Rodríguez (SGIKER, University of the Basque Country) and Professor Pilar Montero (IBERSIMS, University of Granada) for the isotopic and geochronological analyses, respectively, Dr. Teresa Ubide for the editorial work, and two anonymous reviewers for their comments which helped to greatly improve the quality of the original manuscript.

Author contributions AO: conceptualization, methodology, software, formal analysis, validation, investigation, resources, data curation, writing - original draft, writing - review & editing, visualization, project administration. HM: methodology, validation, investigation, resources, data curation, writing - original draft, writing - review & editing, visualization, supervision, project administration. HS'O: methodology, validation, investigation, resources, data curation, writing - original draft, writing - review & editing, visualization.

Funding This work was supported by the Portuguese Foundation for Science and Technology (FCT), through the project ref. UIDB/04683/2020 - ICT (Institute of Earth Sciences). The corresponding author is financially supported by FCT through an individual Ph.D. grant (reference SFRH/BD/138818/2018).

Availability of data and material Not applicable.

Code availability Not applicable.

Declarations

Conflict of interest The authors declare that they have no known competing financial interests or personal relationships that could have appeared to influence the work reported in this paper.

References

Alici Şen, P., Temel, A., & Gourgaud, A. (2004). Petrogenetic modelling of Quaternary post-collisional volcanism: A case study of central and eastern Anatolia. *Geological Magazine, 141*(1), 81–98. https://doi.org/10.1017/S0016756803008550

Allègre, C. J., & Minster, J. F. (1978). Quantitative models of trace element behavior in magmatic processes. *Earth and Planetary Science Letters, 38*(1), 1–25. https://doi.org/10.1016/0012-821X(78)90123-1

Almeida, A., Leterrier, J., Noronha, F., & Bertrand, J. M. (1998). U–Pb zircon and monazite geochronology of the Hercynian two-mica granite composite pluton of Cabeceiras de Basto (Northern Portugal). *Comptes Rendus De L'academie Des Sciences, Serie II, Fascicule a, Earth and Planetary Sciences, 326*(11), 779–785. https://doi.org/10.1016/s1251-8050(98)80243-7

Ballouard, C., Poujol, M., Boulvais, P., Branquet, Y., Tartese, R., & Vigneresse, J. L. (2016). Nb–Ta fractionation in peraluminous granites: A marker of the magmatic-hydrothermal transition. *Geology, 44*(3), 231–234. https://doi.org/10.1130/G37475.1

Batchelor, R. A., & Bowden, P. (1985). Petrogenetic interpretation of granitoid rock series using multicationic parameters. *Chemical Geology, 48*(1–4), 43–55. https://doi.org/10.1016/0009-2541(85)90034-8

Bayat, F., & Torabi, G. (2011). Alkaline lamprophyric province of Central Iran. *Island Arc, 20*, 386–400. https://doi.org/10.1111/j.1440-1738.2011.00776.x

Bea, F., Fershtater, G., & Corretgé, L. G. (1992). The geochemistry of phosphorus in granite rocks and the effect of aluminium. *Lithos, 29*(1–2), 43–56. https://doi.org/10.1016/0024-4937(92)90033-U

Bea, F., Gallastegui, G., Montero, P., Molina, J. F., Scarrow, J., Cuesta, A., & González-Menéndez, L. (2021). Contrasting high-Mg, high-K rocks in Central Iberia: The appinite-vaugnerite conundrum and their (non-existent) relation with arc magmatism. *Journal of Iberian Geology, 47*(1), 235–261. https://doi.org/10.1007/s41513-020-00152-x

Bea, F., Montero, P., & Molina, J. F. (1999). Mafic precursors, peraluminous granitoids, and late lamprophyres in the avila batholith: A model for the generation of variscan batholiths in Iberia. *The Journal of Geology, 107*(4), 399–419. https://doi.org/10.1086/314356

Black, L. P., Kamo, S. L., Allen, C. M., Aleinikoff, J. N., Davis, D. W., Korsch, R. J., & Foudoulis, C. (2003). TEMORA 1: A new zircon standard for phanerozoic U–Pb geochronology. *Chemical Geology, 200*(1–2), 155–170. https://doi.org/10.1016/S0009-2541(03)00165-7

Bonin, B. (1990). From orogenic to anorogenic settings: Evolution of granitoid suites after a major orogenesis. *Geological Journal, 25*(3–4), 261–270. https://doi.org/10.1002/gj.3350250309

Bouchez, J. L., Delas, C., Gleizes, G., Nédélec, A., & Cuney, M. (1992). Submagmatic microfractures in granites. *Geology, 20*(1), 35–38. https://doi.org/10.1130/0091-7613(1992)020%3c0035:SMIG%3e2.3.CO;2

Boynton, W. V. (1984). Geochemistry of the rare earth elements: meteorite studies. In P. Henderson (Ed.), *Rare Earth Element Geochemistry* (pp. 63–114). Elsevier. https://doi.org/10.1016/B978-0-444-42148-7.50008-3

Breiter, K., Frýda, J., & Leichmann, J. (2002). Phosphorus and rubidium in alkali feldspars: case studies and possible genetic interpretations. *Bulletin of the Czech Geological Survey, 77*(2), 93–104. ISSN: 1210-3527

Broska, I., Williams, C. T., Uher, P., Konečný, P., & Leichmann, J. (2004). The geochemistry of phosphorus in different granite suites of the Western Carpathians, Slovakia: The role of apatite and P-bearing feldspar. *Chemical Geology, 205*(1–2), 1–15. https://doi.org/10.1016/j.chemgeo.2003.09.004

Cabanis, B., & Lecolle, M. (1989). Le diagramme La/10-Y/15-Nb/8: un outil pour la discrimination des séries volcaniques et la mise en évidence des processus de mélange et/ou de contamination crustale. *Comptes Rendus De L'académie Des Sciences, Série 2, Mécanique, Physique, Chimie, Sciences De L'univers, Sciences De La Terre, 309*(20), 223–229

Cruz, C.C.F., (2020). *Post-tectonic Variscan magmatism from northwest Iberia. Implications for W-Mo metallogeny. Case study of Lamas de Olo Pluton* (p. 327). Portugal: Faculdade de Ciências da Universidade do Porto (**Thesis submitted for the Ph.D. degree (unpublished thesis)**).

Cruz, C., Góis, J., Sant'Ovaia, H., & Noronha, F. (2020). Geostatistical approach to the study of the magnetic susceptibility variation: Lamas de Olo Pluton case study. *Journal of Iberian Geology, 46*, 279–289. https://doi.org/10.1007/s41513-020-00128-x

Dasgupta, R., Hirschmann, M. M., & Withers, A. C. (2004). Deep global cycling of carbon constrained by the solidus of anhydrous, carbonated eclogite under upper mantle conditions. *Earth and Planetary Science Letters, 227*(1–2), 73–85. https://doi.org/10.1016/j.epsl.2004.08.004

De La Roche, H., Leterrier, J., Grandclaude, P., & Marchal, M. (1980). A classification of volcanic and plutonic rocks using R1–R2 diagrams and major element analysis—its relationships with current nomenclature. *Chemical Geology, 29*(1–4), 183–210. https://doi.org/10.1016/0009-2541(80)90020-0

De Muynck, D., Huelga-Suárez, G., Van Heghe, L., Degryse, P., & Vanhaecke, F. (2009). Systematic evaluation of a strontium-specific extraction chromatographic resin for obtaining a purified Sr fraction with quantitative recovery from complex and Ca-rich matrices. *Journal of Analytical Atomic Spectrometry, 24*(11), 1498–1510. https://doi.org/10.1039/B908645E

Debon, F., & LeFort, P. (1983). A chemical-mineralogical classification of common plutonic rocks and associations. *Earth and Environmental Science Transactions of the Royal Society of Edinburgh, 73*(3), 135–149. https://doi.org/10.1017/S0263593300010117

DePaolo, D. J. (1981). Trace element and isotopic effects of combined wallrock assimilation and fractional crystallization. *Earth and Planetary Science Letters, 53*(2), 189–202. https://doi.org/10.1016/0012-821X(81)90153-9

Dias, R., Ribeiro, A., Romão, J., Coke, C., & Moreira, N. (2016). A review of the arcuate structures in the Iberian Variscides; constraints and genetic models. *Tectonophysics, 681*, 170–194. https://doi.org/10.1016/j.tecto.2016.04.011

Doblas, M., Oyarzun, R., López-Ruiz, J., Cebriá, J. M., Youbi, N., Mahecha, V., Lago, M., Pocoví, A., & Cabanis, B. (1998). Permo-carboniferous volcanism in Europe and northwest Africa: A superplume exhaust valve in the centre of Pangaea? *Journal of African Earth Sciences, 26*(1), 89–99. https://doi.org/10.1016/S0899-5362(97)00138-3

Duggen, S., Hoernle, K., van den Bogaard, P., & Garbe-Schönberg, D. (2005). Post-collisional transition from subduction- to intraplate-type magmatism in the westernmost Mediterranean: Evidence for continental-edge delamination of subcontinental lithosphere. *Journal of Petrology, 46*(6), 1155–1201. https://doi.org/10.1093/petrology/egi013

Errandonea-Martin, J., Sarrionandia, F., Carracedo-Sánchez, M., Ibarguchi, J. I. G., & Eguíluz, L. (2018). Petrography and geochemistry of late- to post-Variscan vaugnerite series rocks and calc-alkaline lamprophyres within a cordierite-bearing monzogranite (Sierra Bermeja Pluton, southern Iberian Massif). *Geologica Acta, 16*(3), 237–255. https://doi.org/10.1344/GeologicaActa2018.16.3.1

Fernandes, S., Gomes, M., Teixeira, R., Corfu, F. (2013). Geochemistry of biotite granites from the Lamas de Olo Pluton, northern Portugal. *Geophysical Research Abstracts*, EGU General Assembly, 15, pp. 1. Retrieved February 24, 2021, from https://ui.adsabs.harvard.edu/#abs/2013EGUGA..1511566F/abstract

Fernández-Suárez, J., Arenas, R., Jeffries, T. E., Whitehouse, M. J., & Villaseca, C. (2006). A U–Pb study of zircons from a lower crustal granulite xenolith of the Spanish Central System: A record of Iberian Lithospheric evolution from the neoproterozoic to the triassic. *The Journal of Geology, 114*(4), 471–483. https://doi.org/10.1086/504180

Finger, F., & Schiller, D. (2012). Lead contents of S-type granites and their petrogenetic significance. *Contributions to Mineralogy and Petrology, 164*(5), 747–755. https://doi.org/10.1007/s00410-012-0771-3

Foley, S., Venturelli, G., Green, D. H., & Toscani, L. (1987). The ultrapotassic rocks: Characteristics, classification, and constraints for petrogenetic models. *Earth-Science Reviews, 24*(2), 81–134. https://doi.org/10.1016/0012-8252(87)90001-8

Förster, H. J., Gottesmann, B., Tischendorf, G., Siebel, W., Rhede, D., Seltmann, R., & Wasternack, J. (2007). Permo-Carboniferous subvolcanic rhyolitic dikes in the western Erzgebirge/Vogtland, Germany: A record of source heterogeneity of post-collisional felsic magmatism. *Neues Jahrbuch Für*

Mineralogie-Abhandlungen: Journal of Mineralogy and Geochemistry, 183(2), 123–147. https://doi.org/10.1127/0077-7757/2007/0064

Frey, F. A., Green, D. H., & Roy, S. D. (1978). Integrated models of basalt petrogenesis: A study of quartz tholeiites to olivine melilitites from south eastern Australia utilizing geochemical and experimental petrological data. *Journal of Petrology, 19*(3), 463–513. https://doi.org/10.1093/petrology/19.3.463

Frost, B. R., Barnes, C. G., Collins, W. J., Arculus, R. J., Ellis, D. J., & Frost, C. D. (2001). A geochemical classification for granitic rocks. *Journal of Petrology, 42*(11), 2033–2048. https://doi.org/10.1093/petrology/42.11.2033

Furman, T., & Graham, D. (1999). Erosion of lithospheric mantle beneath the East African Rift system: Geochemical evidence from the Kivu volcanic province. *Developments in Geotectonics, 24*, 237–262. https://doi.org/10.1016/S0419-0254(99)80014-7

Green, T. H. (1995). Significance of Nb/Ta as an indicator of geochemical processes in the crust-mantle system. *Chemical Geology, 120*(3–4), 347–359. https://doi.org/10.1016/0009-2541(94)00145-X

Harris, N. B. W., Pearce, J. A., & Tindle, A. G. (1986). Geochemical characteristics of collision-zone magmatism. *Geological Society, London, Special Publications, 19*, 67–81. https://doi.org/10.1144/GSL.SP.1986.019.01.04

Helal, B., (1992). *Granitoïdes, granites à métaux rares et hydrothermalisme associe: géologie, minerálogie et geochimie de plusieurs suites tardi-hercyniennes (Nord du Portugal)* (p. 508). France: Ecole Nacionale Supérieure des Mines de Saint-Etienne (**Thesis submitted for the Ph.D. degree** (**unpublished thesis**)).

Hrouda, F. (1985). The magnetic fabric of the Brno Massif. *Sborník Geologických Ved Užitá Geofyzika, 19*, 89–112

Hrouda, F., Verner, K., Kubínová, Š, Buriánek, D., Faryad, S. W., Chlupácová, M., & Holub, F. V. (2016). Magnetic fabric and emplacement of dykes of lamprophyres and related rocks of the Central Bohemian Dyke Swarm (Central European Variscides). *Journal of Geosciences, 61*(4), 335–354. https://doi.org/10.3190/jgeosci.222

Inglis, E. C., Creech, J. B., Deng, Z., & Moynier, F. (2018). High-precision zirconium stable isotope measurements of geological reference materials as measured by double-spike MC-ICPMS. *Chemical Geology, 493*, 544–552. https://doi.org/10.1016/j.chemgeo.2018.07.007

Jacobsen, S. B., & Wasserburg, G. J. (1984). Sm-Nd isotopic evolution of chondrites and achondrites II. *Earth and Planetary Science Letters, 67*(2), 137–150. https://doi.org/10.1016/0012-821X(84)90109-2

Jung, S., Masberg, P., Mihm, D., & Hoernes, S. (2009). Partial melting of diverse crustal sources—constraints from Sr–Nd–O isotope compositions of quartz diorite–granodiorite–leucogranite associations (Kaoko Belt, Namibia). *Lithos, 111*(3–4), 236–251. https://doi.org/10.1016/j.lithos.2008.10.010

Kirstein, L. A., Davies, G. R., & Heeremans, M. (2006). The petrogenesis of Carboniferous-Permian dyke and sill intrusions across northern Europe. *Contributions to Mineralogy and Petrology, 152*(6), 721–742. https://doi.org/10.1007/s00410-006-0129-9

LaFlèche, M. R., Camiré, G., & Jenner, G. A. (1998). Geochemistry of post-Acadian, Carboniferous continental intraplate basalts from the Maritimes Basin, Magdalen Islands, Québec Canada. *Chemical Geology, 148*(3–4), 115–136. https://doi.org/10.1016/S0009-2541(98)00002-3

Lago, M., Arranz, E., Pocoví, A., Galé, C., & Gil-Imaz, A. (2004). Permian magmatism and basin dynamics in the southern Pyrenees: A record of the transition from late Variscan transtension to early Alpine extension. *Geological Society, London, Special Publications, 223*, 439–464. https://doi.org/10.1144/GSL.SP.2004.223.01.19

Le Maitre, R. W., Streckeisen, A., Zanettin, B., Le Bas, M. J., Bonin, B., Bateman, P., Bellieni, G., Dudek, A., Efremova, S., Keller, J., Lameyre, J., Sabine, P. A., Schmid, R., Sorensen, H., & Woolley, A. R. (2002). Igneous rocks: a classification and glossary of terms. *Recommendations of the International Union of Geological Sciences Subcommission on the Systematics of Igneous Rocks.* Cambridge University Press. ISBN: 978-0-511-06864-5

Liew, T. C., & Hofmann, A. W. (1988). Precambrian crustal components, plutonic associations, plate environment of the Hercynian Fold Belt of central Europe: Indications from a Nd and Sr isotopic study. *Contributions to Mineralogy and Petrology, 98*(2), 129–138. https://doi.org/10.1007/BF00402106

Liu, B., Wu, J. H., Li, H., Wu, Q. H., Evans, N. J., Kong, H., & Xi, X. S. (2020). Geochronology, geochemistry and petrogenesis of the Dengfuxian lamprophyres: Implications for the early Cretaceous tectonic evolution of the South China Block. *Geochemistry, 80*(2), 125598. https://doi.org/10.1016/j.chemer.2020.125598

Lorenz, V., & Nicholls, I. A. (1976). The Permocarboniferous Basin and Range Province of Europe: an application op plate tectonics. In H. Falke (Ed.), *The Continental Permian in Central, West, and South Europe. Nato Advanced Study Institutes Series (Series C—Mathematical and Physical Sciences)* (Vol. 22, pp. 313–342). Springer. https://doi.org/10.1007/978-94-010-1461-8_22

Lugmair, G. W., & Marti, K. (1978). Lunar initial ^{143}Nd/^{144}Nd: Differential evolution of the lunar crust and mantle. *Earth and Planetary Science Letters, 39*(3), 349–357. https://doi.org/10.1016/0012-821X(78)90021-3

Ma, L., Jiang, S. Y., Hofmann, A. W., Dai, B. Z., Hou, M. L., Zhao, K. D., Chen, L. H., Li, J. W., & Jiang, Y. H. (2014). Lithospheric and asthenospheric sources of lamprophyres in the Jiaodong Peninsula: A consequence of rapid lithospheric thinning beneath the North China Craton? *Geochimica Et Cosmochimica Acta, 124*, 250–271. https://doi.org/10.1016/j.gca.2013.09.035

McDonough, W. F. (1990). Constraints on the composition of the continental lithospheric mantle. *Earth and Planetary Science Letters, 101*(1), 1–18. https://doi.org/10.1016/0012-821X(90)90119-I

McDonough, W. F., & Sun, S. S. (1995). The composition of the earth. *Chemical Geology, 120*(3–4), 223–253. https://doi.org/10.1016/0009-2541(94)00140-4

Michard, A., Gurriet, P., Soudant, M., & Albarede, F. (1985). Nd isotopes in French Phanerozoic shales: external vs internal aspects of crustal evolution. *Geochimica Et Cosmochimica Acta, 49*(2), 601–610. https://doi.org/10.1016/0016-7037(85)90051-1

Müller, D., Rock, N. M. S., & Groves, D. I. (1992). Geochemical discrimination between shoshonitic and potassic volcanic rocks in different tectonic settings: A pilot study. *Mineralogy and Petrology, 46*, 259–289. https://doi.org/10.1007/BF01173568

Muttoni, G., Kent, D. V., Garzanti, E., Brack, P., Abrahamsen, N., & Gaetani, M. (2003). Early permian pangea 'B' to late permian pangea 'A.' *Earth and Planetary Science Letters, 215*(3–4), 379–394. https://doi.org/10.1016/S0012-821X(03)00452-7

Nédélec, A., & Bouchez, J. L. (2015). *Granites: Petrology, Structure, Geological Setting, and Metallogeny*. Oxford University Press. ISBN: 978-0-19-870561-1

Oliveira, A., Martins, H.C.B., Sant'Ovaia, H., 2019. The Lamas de Olo microgranite and lamprophyre veins: Petrography and Anisotropy of Magnetic Susceptibility. *Livro de Atas do IX Congresso Jovens Investigadores em Geociências*, LEG 2019, Estremoz, 23–24 de novembro de 2019, pp. 23–26

Oliveira, A., Martins, H.C.B., Sant'Ovaia, H. (2020a). Geochemical study of two compositionally contrasting veins of the Lamas de Olo region (Celorico de Basto). *Livro de Atas do X Congresso Jovens Investigadores em Geociências*, LEG 2020, Estremoz, 20 de novembro de 2020, pp. 16–19

Oliveira, A., Martins, H.C.B., Sant'Ovaia, H. (2020b). Insights into the felsic vein magmatism in northern Portugal (Central Iberian

Zone): an integrated geochemical and petrophysical study. In: *20th International Multidisciplinary Scientific GeoConference, SGEM 2020, Conference Proceedings*, *20* (1.1), pp. 139–146. https://doi.org/10.5593/sgem2020/1.1/s01.018, ISBN: 978-619-7603-04-0, ISSN: 1314–2704

Orejana, D., Villaseca, C., Billström, K., & Paterson, B. A. (2008). Petrogenesis of Permian alkaline lamprophyres and diabases from the Spanish Central System and their geodynamic context within western Europe. *Contributions to Mineralogy and Petrology, 156*(4), 477–500. https://doi.org/10.1007/s00410-008-0297-x

Orejana, D., Villaseca, C., & Kristoffersen, M. (2020). Geochemistry and geochronology of mafic rocks from the Spanish Central System: Constraints on the mantle evolution beneath central Spain. *Geoscience Frontiers, 11*(5), 1651–1667. https://doi.org/10.1016/j.gsf.2020.01.002

Patiño Douce, A. E. (1999). What do experiments tell us about the relative contributions of crust and mantle to the origin of granitic magmas? *Geological Society, London, Special Publications, 168*, 55–75. https://doi.org/10.1144/GSL.SP.1999.168.01.05

Peccerillo, A., & Taylor, S. R. (1976). Geochemistry of Eocene calc-alkaline volcanic rocks from the Kastamonu area, northern Turkey. *Contributions to Mineralogy and Petrology, 58*(1), 63–81. https://doi.org/10.1007/BF00384745

Pereira, E. (1989). Notícia Explicativa da Folha 10-A (Celorico de Basto). In: *Carta Geológica de Portugal na Escala 1:50,000*. Serviços Geológicos de Portugal

Pereira, E., Silva, N., Moreira, A., Ribeiro, A. (1987). Folha 10-A (Celorico de Basto). *Carta Geológica de Portugal na Escala 1:50,000*. Serviços Geológicos de Portugal

Perini, G., Cebria, J. M., Lopez-Ruiz, J., & Doblas, M. (2004). Carboniferous-Permian mafic magmatism in the Variscan belt of Spain and France: Implications for mantle sources. *Geological Society, London, Special Publications, 223*(1), 415–438. https://doi.org/10.1144/GSL.SP.2004.223.01.18

Pin, C., & Santos Zalduegui, J. F. (1997). Sequential separation of light rare-earth elements, thorium and uranium by miniaturized extraction chromatography: Application to isotopic analyses of silicate rocks. *Analytica Chimica Acta, 339*(1–2), 79–89. https://doi.org/10.1016/S0003-2670(96)00499-0

Raposo, M. I. B. (2011). Magnetic fabric of the Brazilian dike swarms: a review. In E. Petrovský, D. Ivers, T. Harinarayana, & E. Herrero-Bervera (Eds.), *The Earth's Magnetic Interior. IAGA Special Sopron Book Series* (Vol. 1, pp. 247–262). Springer. https://doi.org/10.1007/978-94-007-0323-0_17

Raposo, M. I. B., & Ernesto, M. (1995). Anisotropy of magnetic susceptibility in the Ponta Grossa dyke swarm (Brazil) and its relationship with magma flow direction. *Physics of the Earth and Planetary Interiors, 87*(3–4), 183–196. https://doi.org/10.1016/0031-9201(94)02970-M

Rock, N. M. S. (1977). The nature and origin of lamprophyres: some definitions, distinctions, and derivations. *Earth-Science Reviews, 13*(2), 123–169. https://doi.org/10.1016/0012-8252(77)90020-4

Rock, N. M. S. (1987). The nature and origin of lamprophyres: An overview. *Geological Society, London, Special Publications, 30*, 191–226. https://doi.org/10.1144/GSL.SP.1987.030.01.09

Rock, N. M. S. (1991). *Lamprophyres*. Blackie. ISBN: 978-1-4757-0931-5

Rubatto, D., & Gebauer, D. (2000). Use of cathodoluminescence for U–Pb zircon dating by ion microprobe: some examples from the western Alps. In M. Pagel, V. Barbin, P. Blanc, & D. Ohnenstetter (Eds.), *Cathodoluminescence in Geosciences* (pp. 373–400). Springer. https://doi.org/10.1007/978-3-662-04086-7_15

Rudnick, R. L., & Fountain, D. M. (1995). Nature and composition of the continental crust: A lower crustal perspective. *Reviews of Geophysics, 33*(3), 267–309. https://doi.org/10.1029/95RG01302

Rudnick, R. L., & Gao, S. (2003). Composition of the continental crust. In H. D. Holland & K. K. Turekian (Eds.), *Treatise on Geochemistry 3: The Crust* (pp. 1–64). Elsevier-Pergamon. ISBN: 0-08-044847-X

Scarrow, J. H., Bea, F., Montero, P., & Molina, J. F. (2008). Shoshonites, vaugnerites and potassic lamprophyres: Similarities and differences between 'ultra'-high-K rocks. *Earth and Environmental Science Transactions of the Royal Society of Edinburgh, 99*(3–4), 159–175. https://doi.org/10.1017/S1755691009008032

Scarrow, J. H., Bea, F., Montero, P., Molina, J. F., & Vaughan, A. P. M. (2006). A precise late Permian ^{40}Ar/^{39}Ar age for Central Iberian camptonitic lamprophyres. *Geologica Acta, 4*(4), 451–459. https://doi.org/10.1344/105.000000346

Scarrow, J. H., Molina, J. F., Bea, F., Montero, P., & Vaughan, A. P. (2011). Lamprophyre dikes as tectonic markers of late orogenic transtension timing and kinematics: A case study from the Central Iberian Zone. *Tectonics, 30*(4), TC4007. https://doi.org/10.1029/2010TC002755

Seifert, T. (2008). *Metallogeny and Petrogenesis of Lamprophyres in the Mid-European Variscides*. IOS Press Millpress. ISBN: 978-1-58603-988-2

Semiz, B., Çoban, H., Roden, M. F., Özpinar, Y., Flower, M. F. J., & McGregor, H. (2012). Mineral composition in cognate inclusions in Late Miocene-Early Pliocene potassic lamprophyres with affinities to lamproites from the Denizli region, Western Anatolia, Turkey: Implications for uppermost mantle processes in a back-arc setting. *Lithos, 134–135*, 253–272. https://doi.org/10.1016/j.lithos.2012.01.005

Sen, G., & Leeman, W. P. (1991). Iron-rich lherzolitic xenoliths from Oahu: Origin and implications for Hawaiian magma sources. *Earth and Planetary Science Letters, 102*(1), 45–57. https://doi.org/10.1016/0012-821X(91)90016-B

Shaw, D. M. (1970). Trace element fractionation during anatexis. *Geochimica Et Cosmochimica Acta, 34*(2), 237–243. https://doi.org/10.1016/0016-7037(70)90009-8

Shaw, A. M., Hilton, D. R., Fischer, T. P., Walker, J. A., & Alvarado, G. E. (2003). Contrasting He–C relationships in Nicaragua and Costa Rica: Insights into C cycling through subduction zones. *Earth and Planetary Science Letters, 214*(3–4), 499–513. https://doi.org/10.1016/S0012-821X(03)00401-1

Soder, C. G., & Romer, R. L. (2018). Post-collisional potassic–ultrapotassic magmatism of the variscan orogen: implications for mantle metasomatism during continental subduction. *Journal of Petrology, 59*(6), 1007–1034. https://doi.org/10.1093/petrology/egy053

Štemprok, M., Dolejš, D., & Holub, F. V. (2014). Late Variscan calc-alkaline lamprophyres in the Krupka ore district, Eastern Krušné hory/Erzgebirge: Their relationship to Sn–W mineralization. *Journal of Geosciences, 59*(1), 41–68. https://doi.org/10.3190/jgeosci.156

Štemprok, M., Dolejš, D., Müller, A., & Seltmann, R. (2008). Textural evidence of magma decompression, devolatilization and disequilibrium quenching: An example from the Western Krušné hory/Erzgebirge granite pluton. *Contributions to Mineralogy and Petrology, 155*(1), 93–109. https://doi.org/10.1007/s00410-007-0229-1

Sun, S. S., & McDonough, W. F. (1989). Chemical and isotopic systematics of oceanic basalts: Implications for mantle composition and processes. *Geological Society, London, Special Publications, 42*, 313–345. https://doi.org/10.1144/GSL.SP.1989.042.01.19

Sylvester, P. J. (1998). Post-collisional strongly peraluminous granites. *Lithos, 45*(1–4), 29–44. https://doi.org/10.1016/S0024-4937(98)00024-3

Teixeira, R.J.S. (2008). *Mineralogia, petrologia e geoquímica dos granitos e seus encraves da região de Carrazeda de Ansiães* (p. 463). Portugal: Universidade de Trás-os-Montes e Alto Douro **(Thesis submitted for the Ph.D. degree (unpublished thesis))**.

Timmerman, M. J. (2004). Timing, geodynamic setting and character of Permo-Carboniferous magmatism in the foreland of the Variscan Orogen, NW Europe. *Geological Society, London, Special Publications, 223*(1), 41–74. https://doi.org/10.1144/GSL.SP.2004.223.01.03

Ubide, T., Lago, M., Arranz, E., Galé, C., & Larrea, P. (2010). The lamprophyric sub-vertical dyke swarm from Aiguablava (Catalonian Coastal Ranges): petrology and composition. *Geogaceta, 49*, 83–86. ISSN: 2173-6545

Vernon, R. H. (2004). *A Practical Guide to Rock Microstructure*. Cambridge University Press, UK. ISBN: 052181443X

Villa, I. M., De Bièvre, P., Holden, N. E., & Renne, P. R. (2015). IUPAC-IUGS recommendation on the half-life of ^{87}Rb. *Geochimica Et Cosmochimica Acta, 164*, 382–385. https://doi.org/10.1016/j.gca.2015.05.025

Villaseca, C., Barbero, L., & Herreros, V. (1998). A re-examination of the typology of peraluminous granite types in intracontinental orogenic belts. *Transactions of the Royal Society of Edinburgh Earth Sciences, 89*, 113–119. https://doi.org/10.1017/S0263593300007045

Villaseca, C., Orejana, D., Pin, C., López-Garcia, J. A., & Andonaegui, P. (2004). Le magmatisme basique hercynien et post-hercynien du Système central espagnol: essai de caractérisation des sources mantelliques. *Comptes Rendus Geoscience, 336*(10), 877–888. https://doi.org/10.1016/j.crte.2004.02.008

Wilson, M. (1989). *Igneous Petrogenesis*. Springer. https://doi.org/10.1007/978-1-4020-6788-4. ISBN: 978-1-4020-6788-4

Wu, F., Liu, X., Ji, W., Wang, J., & Yang, L. (2017). Highly fractionated granites: Recognition and research. *Science China Earth Sciences, 60*(7), 1201–1219. https://doi.org/10.1007/s11430-016-5139-1

Zeng, R., Lai, J., Mao, X., Xiao, W., Yan, J., Zhang, C., Hu, J., & Ai, Q. (2020). Petrogenesis and tectonic significance of the Early Devonian lamprophyres and diorites in the Alxa Block NW China. *Geochemistry*. https://doi.org/10.1016/j.chemer.2020.125685